Diagnosis of the Three-Dimensional Circulation in Mesoscale Features with Large Rossby Number

R. KIPP SHEARMAN,* JOHN A. BARTH, AND J. S. ALLEN

College of Oceanic and Atmospheric Sciences, Oregon State University, Corvallis, Oregon

ROBERT L. HANEY

Department of Meteorology, Naval Postgraduate School, Monterey, California

(Manuscript received 5 January 1999, in final form 8 December 1999)

ABSTRACT

Several diagnoses of three-dimensional circulation, using density and velocity data from a high-resolution, upper-ocean SeaSoar and acoustic Doppler current profiler (ADCP) survey of a cyclonic jet meander and adjacent cyclonic eddy containing high Rossby number flow, are compared. The Q-vector form of the quasigeostrophic omega equation, two omega equations derived from iterated geostrophic intermediate models, an omega equation derived from the balance equations, and a vertical velocity diagnostic using a primitive equation model in conjunction with digital filtering are used to diagnose vertical and horizontal velocity fields. The results demonstrate the importance of the gradient wind balance in flow with strong curvature (high Rossby number). Horizontal velocities diagnosed from the intermediate models (the iterated geostrophic models and the balance equations), which include dynamics between those of quasigeostrophy and the primitive equations, are significantly reduced (enhanced) in comparison with the geostrophic velocities in regions of strong cyclonic (anticyclonic) curvature, consistent with gradient wind balance. The intermediate model relative vorticity fields are functionally related to the geostrophic relative vorticity field; anticyclonic vorticity is enhanced and cyclonic vorticity is reduced. The iterated geostrophic, balance equation and quasigeostrophic vertical velocity fields are similar in spatial pattern and scale, but the iterated geostrophic (and, to a lesser degree, the balance equation) vertical velocity is reduced in amplitude compared with the quasigeostrophic vertical velocity. This reduction is consistent with gradient wind balance, and is due to a reduction in the forcing of the omega equation through the geostrophic advection of ageostrophic relative vorticity. The vertical velocity diagnosed using a primitive equation model and a digital filtering technique also exhibits reduced magnitude in comparison with the quasigeostrophic field. A method to diagnose the gradient wind from a given dynamic height field has been developed. This technique is useful for the analysis of horizontal velocity in the presence of strong flow curvature. Observations of the nondivergent ageostrophic velocity field measured by the ADCP compare closely with the diagnosed gradient wind ageostrophic velocity.

1. Introduction

The seasonally energetic California Current system (CCS) often exhibits sharp frontal features, such as cold filaments, particularly during upwelling season (Strub et al. 1991). Strong fronts in the density field are accompanied by large alongfront geostrophic currents and large relative vorticities (Kosro and Huyer 1986; Onken et al. 1990). Associated with fronts and strong geostrophic currents are potentially sizable secondary or ageostrophic circulations, including vertical motion. Ageostrophic circulation at a front is required to offset the tendency for thermal wind to destroy itself (Hoskins et al. 1978).

Determination of the three-dimensional circulation associated with mesoscale features is complicated, primarily by our inability to accurately measure the vertical velocity w. Hence, indirect methods for estimating w from observable fields are required. In the absence of information about temporal evolution, the Q-vector form of the quasigeostrophic (QG) omega equation (Hoskins et al. 1978) is a useful technique for diagnosing the vertical circulation from the observed, synoptic density and geostrophic velocity fields, such as provided by a single hydrographic survey. Recently, the QG diagnosis of three-dimensional circulation has been successfully applied to oceanic datasets (Viúdez et al.

* Current affiliation: Department of Physical Oceanography, Woods Hole Oceanographic Institution, Woods Hole, Massachusetts.

Corresponding author address: Dr. R. Kipp Shearman, Woods Hole Oceanographic Institution, Dept. of Physical Oceanography, Woods Hole, MA 02543.
E-mail: kshearman@whoi.edu

1996; Rudnick 1996; Allen and Smeed 1996; Shearman et al. 1999).

The applicability of QG dynamics to mesoscale features is limited in the presence of large Rossby number flow. Hence, the QG diagnostic methods may not accurately represent the vertical velocity field in mesoscale features with large Rossby numbers. Primitive equation (PE) models offer a more comprehensive set of dynamics. The complexity of the PE model, however, is sometimes a hindrance in isolating particular physical processes. Intermediate models, such as the geostrophic momentum approximation (Hoskins 1975), the semigeostrophic equations (Hoskins and Draghici 1977), the balance equations (Gent and McWilliams 1983), and iterated geostrophic models (Allen 1993), were developed as a means for incorporating dynamics between QG and PE. Diagnostic methods for estimating ageostrophic circulations based on intermediate models should therefore have improved accuracy compared with QG diagnostics.

This paper builds upon the work of Shearman et al. (1999), who diagnosed, via the Q-vector form of the quasigeostrophic omega equation, the three-dimensional circulation associated with a cyclonic jet meander and adjacent cyclonic eddy in the CCS. Density and velocity data from small-scale survey 1 (SS1), a high-resolution upper-ocean SeaSoar/Acoustic Doppler Current Profiler (ADCP) survey conducted as part of the 1993 Eastern Boundary Currents (EBC) program (Huyer et al. 1998), were objectively analyzed to form smooth, gridded fields (2 km horizontal and 10 m vertical spacing) from which the geostrophic horizontal and quasigeostrophic vertical flow fields were diagnosed. The data reduction procedures are described in Shearman et al. (1999). For the SeaSoar density, a spatially variable mean field is determined by fitting a second-order polynomial to the SeaSoar observations. The fitted mean is then removed and the residual objectively analyzed (Bretherton et al. 1976) using the correlation function (decay scale and zero crossing of ~20 km) reported in Shearman et al. (1999). The data reduction procedure for the ADCP data is similar with the additional constraint of nondivergence.

Corresponding to the position of the jet meander, a cold filament can be seen in sea surface temperature (Fig. 1) making a sharp cyclonic turn in the SS1 survey region. The ship track for SS1 relative to this feature is also shown (Fig. 1), demonstrating the high spatial resolution of this survey. The SS1 density field (Fig. 2) was characterized by a curvilinear front that follows approximately the same cyclonic path as the surface filament. As reported by Shearman et al. (1999) the density front was strongest between 70 and 100 m and weakened below these depths. The geostrophic velocity field, referenced to the objectively analyzed ADCP data at 200 m (constrained through the objective analysis to be nondivergent), showed a surface-intensified jet with a maximum speed of 0.9 m s^{-1} that followed the density front along the cyclonic meander. Geostrophic relative vorticity within the jet ranged from $-0.8f$ to $1.2f$ at the surface, where f is the local Coriolis parameter. The diagnosed quasigeostrophic vertical velocity field was characterized by two length scales: a large (~75 km) pattern of downwelling upstream and upwelling downstream of the primary cyclonic bend; and smaller (20–30 km) patches associated with similar scale meanders in the jet. The maximum vertical velocity was 40–45 m d^{-1} and was found within the jet between depths of 70–100 m.

The objectives of this paper are to compare existing methods and to develop techniques that are more accurate than QG for diagnosing three-dimensional circulation in the presence of large Rossby number flow. In addition, the dynamics of mesoscale features are examined, emphasizing the importance of the gradient wind balance in features with strong flow curvature.

The remainder of this paper is organized as follows: Section 2 describes the intermediate models (the iterated geostrophic models and the balance equations) and the development of the associated horizontal and vertical velocity diagnostics; section 3 covers the diagnosis of three-dimensional circulation using the primitive equations and digital filter initialization technique; section 4 (along with appendix A) recapitulates gradient wind theory and describes a method for diagnosing the gradient wind from a synoptic dynamic height field; section 5 discusses the results of the different diagnostic techniques vis-à-vis the gradient wind balance; and section 6 summarizes the preceding material.

2. Intermediate models

Intermediate models contain physics between quasigeostrophy and the primitive equations. They are therefore capable of representing oceanic flows with strong velocities, steep isopycnal slopes, and a wide range of Rossby number ($0 < \varepsilon < 1$) more accurately than QG. Intermediate models also have the benefit of dynamically filtering transient high-frequency inertia–gravity waves, which are contained in the PE solutions and can obscure the dynamically relevant, more slowly evolving mesoscale circulation. The balance equations (Gent and McWilliams 1983) and the iterated geostrophic models (Allen 1993) are examples of intermediate models. They are used here to derive diagnostics of the three-dimensional circulation associated with a sharp cyclonic jet meander and adjacent cyclonic eddy in the CCS. The meander and eddy exhibit strong horizontal velocities (~1 m s^{-1}) and large relative vorticities (~$1f$), which imply a large Rossby number (~ 1). The QG approximation is less applicable in these circumstances, and the intermediate models more appropriate.

a. Iterated geostrophic model IG1

Iterated geostrophic models (denoted IG*n* where *n* is the iteration number), developed by Allen (1993), con-

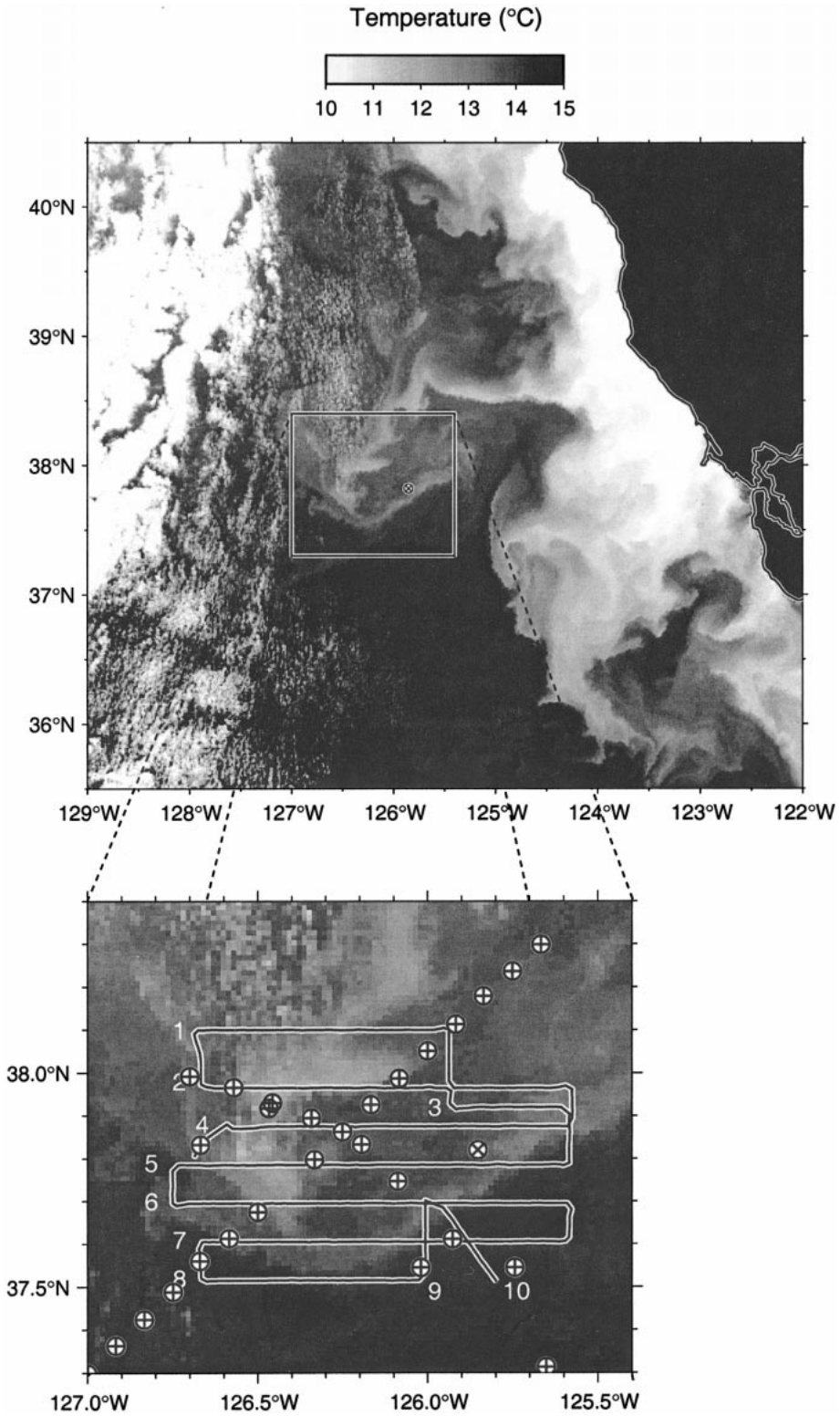

FIG. 1. (top) Satellite SST image (2300 UTC 29 Jun 1993) of the SS1 survey region, showing a filament of cold water, associated with a strong current jet and density front, making a sharp cyclonic turn. (bottom) The SS1 survey region is expanded, and the shiptrack for SS1 is overlaid. The ⊕ indicate the locations of CTD casts used to determine extended dataset, and the ⊗ indicates the current meter mooring location.

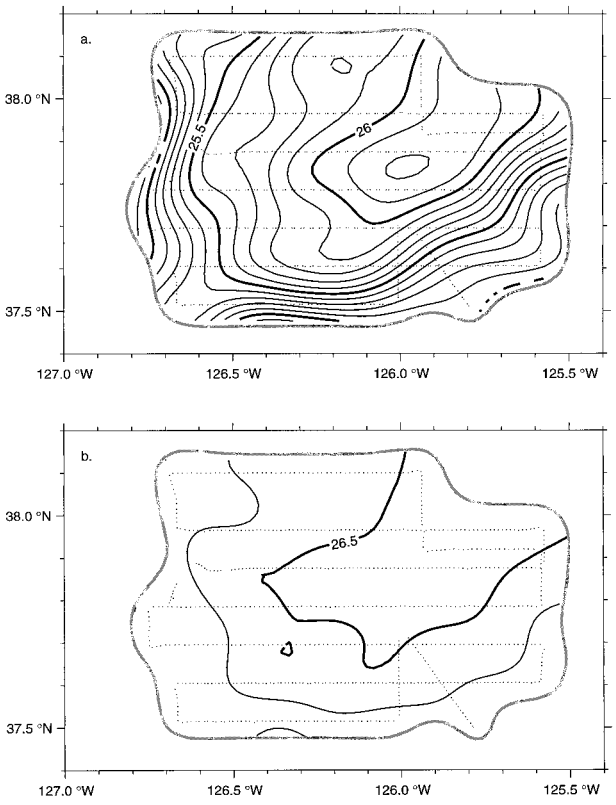

FIG. 2. SS1 objectively analyzed σ_t (kg m^{-3}) at (a) 100 m and (b) 200 m. Contour interval is 0.1 kg m^{-3}. The region within the thick gray contour has an error covariance (from the objective analysis) of less than 10% of the raw data variance. Observation data points are indicated by the small black dots.

tain physics between quasigeostrophy and the primitive equations. Iterated geostrophic models provide a systematic method for extending model dynamics to higher order in Rossby number. IG0 is the geostrophic balance, and the subsequent iterated geostrophic models expand upon the geostrophic balance to increase the model's accuracy in powers of Rossby number. The inviscid, f-plane relationships between model iterations, where all variables are nondimensional and n again signifies the iteration number, are given by [Eqs. (7a–c) in Allen 1993]

$$u_{n+1} = -\phi_y + \varepsilon[-v_{nt} - \zeta_n u_n - K_{ny}] - \varepsilon^2 w_n v_{nz}, \quad (1)$$

$$v_{n+1} = \phi_x + \varepsilon[u_{nt} - \zeta_n v_n - K_{nx}] - \varepsilon^2 w_n u_{nz}, \quad (2)$$

$$w_{n+1} = -S^{-1}[\phi_{ntz} + \nabla \cdot (\mathbf{u}_n \phi_z) + \varepsilon(w_n \phi_z)_z], \quad (3)$$

where the subscripts x, y, z, and t indicate partial derivatives and ∇ is the horizontal gradient operator. The Rossby number ε is defined as

$$\varepsilon = \frac{U}{fL}, \quad (4)$$

where U, L, and f are the characteristic velocity and lengths scales and local Coriolis parameter, respectively. The horizontal velocity is $\mathbf{u} = (u, v)$ and the three-dimensional velocity is $\mathbf{u}_{3d} = (u, v, \varepsilon w)$, where u, v, εw are the nondimensional eastward, northward, and vertical velocity components, respectively. The pressure field is ϕ, $\zeta = \mathbf{k} \cdot \nabla \times \mathbf{u}$ is the vertical component of relative vorticity ($\mathbf{k}$ is the unit vertical vector), $K = \frac{1}{2}(u^2 + v^2)$ is the kinetic energy per unit mass, and

$$S(z) = \frac{N^2(z)H^2}{L^2 f^2},$$

where H is the characteristic height scale, is the nondimensional Burger number, based on the buoyancy frequency $N(z)$. The following derivation of iterated geostrophic three-dimensional circulation diagnostics uses nondimensional variables. The principal diagnostic equations used in this paper are given in dimensional form in appendix B.

The zero-order geostrophic balance is defined as

$$u_0 = -\phi_y, \qquad v_0 = \phi_x, \qquad w_0 = 0. \quad (5)$$

Note that there is no zero subscript on the pressure field, which is assumed to be known and is not expanded in ε. The tendency (time derivative) of the pressure field, however, is expanded in ε. Consequently, the tendency of the geostrophic pressure field is denoted ϕ_{0t}. The horizontal momentum and density equations in IG1 are the same as in QG:

$$v_1 = \phi_x + \varepsilon[-\phi_{0ty} - J(\phi, \phi_y)], \quad (6)$$

$$u_1 = -\phi_y + \varepsilon[-\phi_{0tx} - J(\phi, \phi_x)], \quad (7)$$

$$Sw_1 = -\phi_{0tz} - J(\phi, \phi_z), \quad (8)$$

where $J(a, b) = a_x b_y - a_y b_x$ is the Jacobian operator. Likewise, the IG1 omega equation is identical to the QG omega equation ($w_1 = w_{qg}$). The IG1 omega equation is derived from the IG1 density equation (8) and vorticity equation, formed by taking the curl of the momentum equations (6) and (7),

$$w_{1z} = \nabla^2 \phi_{0t} + J(\phi, \nabla^2 \phi), \quad (9)$$

where $\nabla^2 \phi = \zeta_0$ and $\nabla^2 \phi_{0t} = \zeta_{0t}$. The continuity equation

$$\nabla \cdot \mathbf{u}_1 = \varepsilon \nabla^2 \chi_1 = -\varepsilon w_{1z}, \quad (10)$$

where χ_1 is the IG1 divergent velocity potential function, has been used to replace horizontal divergence with the vertical derivative of the vertical velocity on the left-hand side (lhs) of (9). The time derivative of the pressure field can be eliminated by adding ∂_z (9) and ∇^2 (8). This yields the nondimensional IG1 omega equation

$$\nabla^2 Sw_1 + w_{1zz} = \partial_z J(\phi, \nabla^2 \phi) - \nabla^2 J(\phi, \phi_z). \quad (11)$$

The first term on the right-hand side (rhs) is referred to as the differential vorticity advection (Holton 1992) and represents the contribution to vertical velocity caused by the stretching and compression of vortex tubes, re-

quired by the conservation of potential vorticity in response to the advection of geostrophic relative vorticity. The second term on the rhs is the negative Laplacian of thickness advection, which is proportional to thickness advection itself (Holton 1992), and represents the contribution to vertical velocity caused by the direct displacement of isopycnals. The forcing of the IG1 omega equation (11) can be reformulated into the nondimensional Q-vector form (Hoskins et al. 1978),

$$\nabla^2 S w_1 + w_{1zz} = \nabla \cdot \mathbf{Q}_1,$$

$$\mathbf{Q}_1 = -2(\mathbf{u}_{0x} \cdot \nabla\theta, \mathbf{u}_{0y} \cdot \nabla\theta), \quad (12)$$

where θ is the negative perturbation density, such that the total nondimensional density field is given by

$$\rho(x, y, z, t) = \rho_0 + \overline{\rho}(z) - \theta(x, y, z, t).$$

The Q-vector form of the QG omega equation has been applied to oceanic datasets previously (Viúdez et al. 1996; Rudnick 1996; Allen and Smeed 1996; Shearman et al. 1999). The solution procedure for the QG/IG1 omega equation follows Shearman et al. (1999). The horizontal boundaries of the computational region are moved away from the area of interest. This should minimize the influence of the lateral boundary conditions, which are $w_x = 0$ on the east–west boundaries and $w_y = 0$ on the north–south boundaries. Furthermore, the divergence of **Q** is set to zero outside of the 0.1 error covariance contour (denoted by the thick gray line in Fig. 2). The boundary condition at the surface is $w = 0$, and at the bottom of the computational region the boundary condition is $w_z = 0$. A slight change has been instituted here in anticipation of the application of the PE/DFI (digital filter initialization) vertical velocity diagnosis, which uses $w = 0$ at a flat, solid bottom boundary. The bottom boundary of the computational region has been extended from 310 m to 510 m to isolate the results obtained in the upper 310 m from the influence of the bottom boundary condition.

Coarse resolution, nonsynoptic, deep hydrographic data from an EBC cruise (Kosro et al. 1995) were used to extend the SS1 SeaSoar density data below 310 m. Twenty-seven conductivity–temperature–depth (CTD) casts to at least 500 m were conducted between 9 May 93 and 11 July 93. The sampling pattern forms a cross, intersecting the curved density front (Fig. 2) at three separate places. The CTD data were gridded using standard objective analysis following Shearman et al. (1999) with historical covariance parameters $a = 55$ km and $b = 120$ km (Walstad et al. 1991). Although the sampling pattern resolves only the coarse length scales and the data are not synoptic, this is not detrimental to the analysis. In the IG diagnoses, the CTD data will only be used to extend the bottom boundary away from the high-resolution, quasi-synoptic SeaSoar data region. As with the lateral boundary conditions, the forcing of the omega equation is set to zero outside of the SeaSoar data region (below 310 m). This technique is similar to extending the density data assuming a constant N^2 (Rudnick 1996), but is preferable since it is based on actual data. For SS1, extension using constant N^2 gives unrealistic densities and maintains the horizontal density gradients from 310 m on down. This is not an issue for the diagnosis of vertical velocity using the omega equation, since the rhs forcing is set to zero in the extended data region. However, in the PE/DFI diagnosis, the large density gradients in the deep region yield unrealistically large geostrophic velocities, and the diagnosis is obviously affected. By using actual data to extend the density field, these problems are avoided.

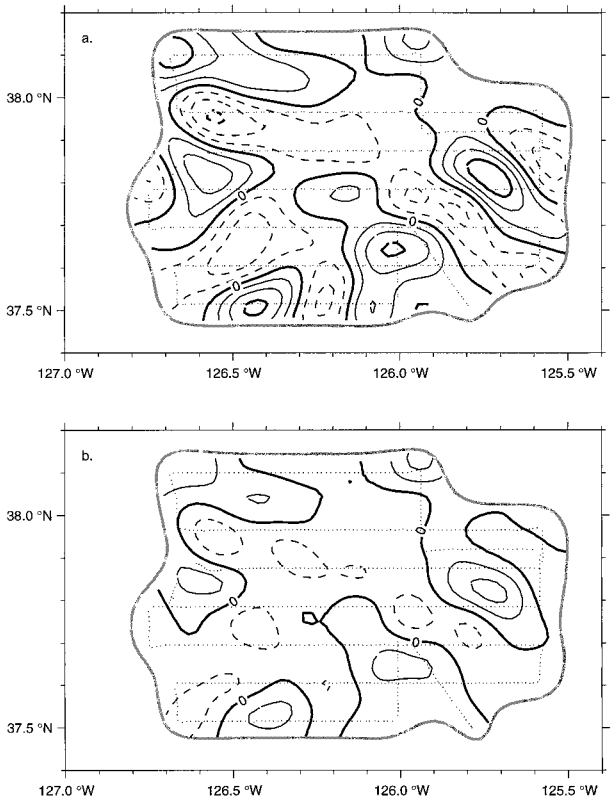

FIG. 3. QG/IG1 vertical velocity w_1 (m d^{-1}) diagnosed from the dimensional form of (12) at (a) 100 and (b) 200 m. Contour interval is 10 m d^{-1} with thick contours -30, 0, and 30 m d^{-1}.

The dimensional QG/IG1 vertical velocity field ($w_1 = w_{qg}$) (Fig. 3) has been diagnosed by solving the dimensional form for (12), using the above boundary conditions. A complete description of the QG vertical velocity field for SS1 is given in Shearman et al. (1999). The rms difference between the QG/IG1 vertical velocity w_{qg} diagnosed using the extended boundary condition $w_z = 0$ at 510 m and the w_{qg} field diagnosed using $w_z = 0$ at 310 m (i.e., as used in Shearman et al. 1999) is 0.8 m d^{-1}, whereas the rms of w_1 itself is 9.4 m d^{-1}.

Once the QG/IG1 vertical velocity has been calculated, the complete (geostrophic and ageostrophic) IG1 horizontal velocity can be diagnosed. The IG1 horizon-

tal velocity field can be separated into its rotational and divergent components

$$\mathbf{u}_1 = \mathbf{u}_{1R} + \varepsilon\mathbf{u}_{1D} = \mathbf{k} \times \nabla\psi_1 + \varepsilon\nabla\chi_1,$$

where $\mathbf{u}_{1R}$ and $\mathbf{u}_{1D}$ are the rotational and divergent velocity components determined from the IG1 streamfunction ψ_1 and velocity potential χ_1, respectively, and $\mathbf{k}$ is the unit vertical vector. The rotational IG1 velocity field is calculated from the divergence of the momentum equations (6) and (7)

$$\nabla^2\psi_1 = \nabla^2\phi - \varepsilon 2J(\phi_x, \phi_y). \tag{13}$$

Since $\nabla^2\psi_1 = \zeta_1$ and $\nabla^2\phi = \zeta_0$, this expression can also be written as a relationship for the IG1 relative vorticity

$$\zeta_1 = \zeta_0 + \varepsilon 2J(v_0, u_0). \tag{14}$$

The ageostrophic relative vorticity is therefore given by $\varepsilon 2J(v_0, u_0)$, which has been identified previously by Keyser et al. (1992). The elliptic operator in (13) is inverted using successive overrelaxation and the boundary condition

$$\mathbf{n} \cdot (\mathbf{k} \times \nabla\psi_1) = \mathbf{n} \cdot \mathbf{u}_0, \tag{15}$$

where $\mathbf{n}$ is the unit normal vector pointing out of the boundary. Using the geostrophic velocity in the boundary condition is formally an approximation to the actual boundary condition, as evident in the IG1 momentum equations (7) and (6). However, since the lateral boundaries are far away from the region of interest, the neglect of higher-order terms in the boundary condition will not make a significant difference. The IG1 rotational velocity field and streamfunction show both the large-scale cyclonic and small-scale meanders exhibited by the geostrophic velocity field and dynamic height (Fig. 4a). The maximum speed in the IG1 rotational velocity field is 0.80 m s^{-1}, which is less than the maximum geostrophic speed of 0.90 m s^{-1}.

Once the QG/IG1 vertical velocity field has been diagnosed from (12), the divergent velocity field can be determined from the dimensional form of the continuity equation (10). There are no obvious physical boundary conditions for this relationship when the lateral boundaries are open. Therefore, the dimensional form of (10) was solved for χ_1 using both Dirichlet and Neumann boundary conditions. The solutions had an rms difference of ~0.001 m s^{-1} compared with a mean divergent velocity of ~0.01 m s^{-1}. For the following analysis, the Neumann boundary condition was used. The divergent velocity field and velocity potential (Fig. 4b) indicate a large-scale convergence toward the center of the cyclonic low. There are also smaller-scale convergent and divergent features, for example, the region of divergence within the downwelling patch at 37.65°N, 126.5°W and the region of convergence within the upwelling patch at 37.6°N, 126.0°W. The divergent velocity field at 100 m (Fig. 4b) is in general below the depth of maximum vertical velocity, thus divergence (convergence) at depth within a downwelling (upwelling) patch is consistent with the intuitive expectation of surface convergence (divergence) leading to downwelling (upwelling) followed by divergence (convergence) at depth. The divergent velocity field is strongest near the surface with speeds of up to 0.1 m s^{-1}.

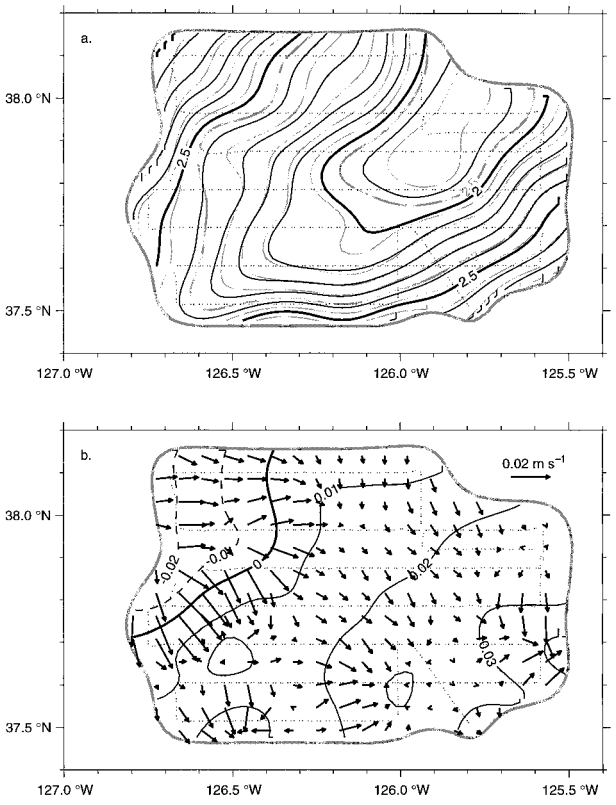

FIG. 4. At 100 m, (a) IG1 streamfunction ψ_1 scaled by f (m^2 s^{-2}) computed from (13) and absolute dynamic height (m^2 s^{-2}) (gray contours); and (b) IG1 velocity potential χ_1 scaled by f (m^2 s^{-2}) and divergent velocity vectors $\mathbf{u}_{1D}$ computed from (10).

b. *Iterated geostrophic model IG2*

The derivation of the IG2 omega equation follows the same steps as the QG/IG1 omega equation. The IG2 vorticity and density equations [(3.30a,b) and (3.24c) in Allen (1993)] are written as

$$w_{2z} = \nabla^2\phi_{1t} + J(\psi_1, \zeta_1) + \varepsilon\{\zeta'_{1t} + \nabla \cdot [w_1\nabla\psi_{1z} + \zeta_1\nabla\chi_1]\} + \varepsilon^2 J(w_1, \chi_{1z}), \tag{16}$$

$$Sw_2 = -\phi_{1tz} - J(\psi_1, \phi_z) - \varepsilon[\nabla \cdot (\phi_z\nabla\chi_1) + (w_1\phi_z)_z], \tag{17}$$

where

$$\zeta_{1t} = \zeta_{0t} + \varepsilon\zeta'_{1t} \quad \text{and} \tag{18}$$

$$\zeta'_{1t} = -2[J(\phi_{0tx}, \phi_y) + J(\phi_x, \phi_{0ty})], \tag{19}$$

recall that $\nabla^2\psi_1 = \zeta_1$ and $\nabla^2\phi = \zeta_0$. To eliminate the time derivative of the IG1 pressure field ϕ_1, take ∂_z (16) and ∇^2 (17), and add to get the IG2 omega equation:

$$\begin{aligned}\nabla^2 S w_2 + w_{2zz} = {} & \partial_z J(\psi_1, \zeta_1) - \nabla^2 J(\psi_1, \phi_z) \\ & + \varepsilon\{\partial_z[\zeta'_{1t} + \boldsymbol{\nabla}\cdot(w_1\boldsymbol{\nabla}\psi_{1z}) + \boldsymbol{\nabla}\cdot(\zeta_1\boldsymbol{\nabla}\chi_1)] \\ & - \nabla^2[\boldsymbol{\nabla}\cdot(\phi_z\boldsymbol{\nabla}\chi_1) + (w_1\phi_z)_z]\} \\ & + \varepsilon^2\{\partial_z J(w_1, \chi_{1z})\}. \end{aligned} \quad (20)$$

Once the IG1 solution is obtained, the rhs of the IG2 omega equation is completely determined in the same way that the rhs of the QG/IG1 omega equation is completely determined by the IG0 or geostrophic solution. The values of ϕ_{0tx} and ϕ_{0ty} in (19) are computed from the IG1 momentum equations (6) and (7). A corresponding Q-vector form for the IG2 omega equation has not been found.

Without the $O(\varepsilon)$ and $O(\varepsilon^2)$ terms, the IG2 omega equation is identical to the QG omega equation (11) with the geostrophic advecting velocity and geostrophic relative vorticity replaced by the IG1 rotational velocity and relative vorticity

$$\nabla^2 S w_2^{2d} + w_{2zz}^{2d} = \partial_z J(\psi_1, \nabla^2\psi_1) - \nabla^2 J(\psi_1, \phi_z), \quad (21)$$

where the superscript $2d$ denotes the limitation to horizontal advection on the rhs. This clipped forcing has the same contributing terms as the QG/IG1 omega equation (horizontal advection of relative vorticity and thickness); however, the advecting velocity is the IG1 rotational velocity field and the advected relative vorticity field is the IG1 relative vorticity. The IG2 diagnosis differs from the geostrophic momentum approximation in that the advection of ageostrophic relative vorticity contributes to the forcing of vertical motion. Likewise, the clipped forcing for the IG2 omega equation differs from the QG/IG1 omega equation through the inclusion of the geostrophic advection of ageostrophic relative vorticity and the nondivergent ageostrophic advection of thickness and relative vorticity (both geostrophic and ageostrophic).

The full rhs of the IG2 omega equation (20) can be reformulated to emphasize the three-dimensional advection of relative vorticity and thickness

$$\begin{aligned}\nabla^2 S w_2 + w_{2zz} = {} & \partial_z(\mathbf{u}_{3d1}\cdot\boldsymbol{\nabla}_{3d}\zeta_1) - \nabla^2(\mathbf{u}_{3d1}\cdot\boldsymbol{\nabla}_{3d}\theta) \\ & + \varepsilon\{\partial_z[\zeta'_{1t} + \mathbf{k}\cdot(\boldsymbol{\nabla}w_1\times\mathbf{u}_{1z}) - \zeta_1 w_{1z}]\}, \end{aligned} \quad (22)$$

where $\boldsymbol{\nabla}_{3d}$ is the three-dimensional gradient operator. Note, the $O(\varepsilon^2)$ term from (20) has been incorporated into the $O(\varepsilon)$ terms, and similarly some $O(\varepsilon)$ terms from (20) have been incorporated into the $O(1)$ expressions, through the use of the total IG1 velocity

$$\mathbf{u}_{3d1} \equiv (u_{1R} + \varepsilon u_{1D},\ v_{1R} + \varepsilon v_{1D},\ \varepsilon w_1).$$

In the full IG2 omega equation, the advection terms are three-dimensional. In addition to the geostrophic and ageostrophic horizontal advection terms included in the clipped forcing, the full IG2 omega equation includes advection of relative vorticity and thickness by the divergent velocity field (u_{1D}, v_{1D}, w_1). The three additional forcing terms in (22) are related to the evolution of the absolute IG1 vorticity field through the baroclinic production (solenoidal), tilting/twisting and divergence terms in the vorticity equation (see Pedlosky 1987). This formulation highlights the utility of the iterated geostrophic intermediate models. At each iteration, the physics are systematically made more inclusive, and each new term is easily identifiable. The solution procedure for both IG2 omega equations (21) and (22) implemented here uses the identical boundary conditions as the QG/IG1 solution.

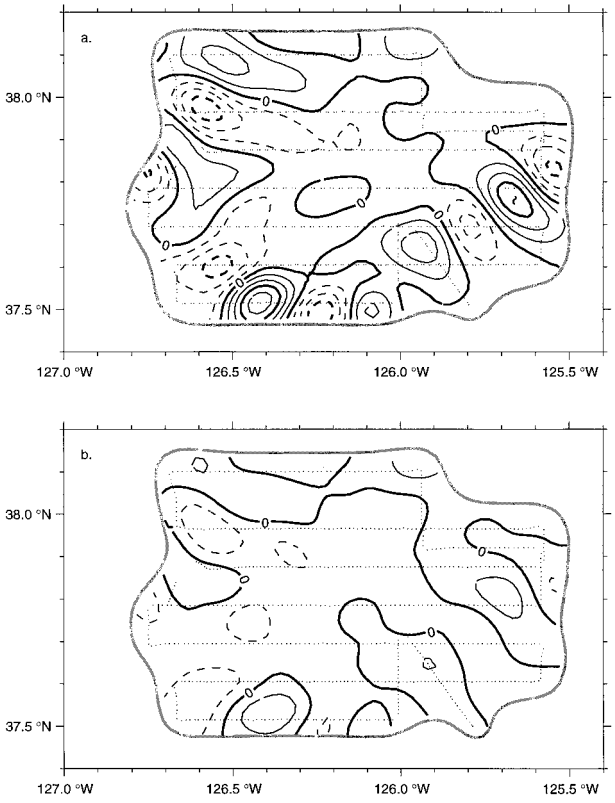

FIG. 5. IG2 vertical velocity w_2^{2d} (m d^{-1}) diagnosed using (21), which includes only the O(1) terms on the rhs of the full IG2 omega equation, at (a) 100 and (b) 200 m. Contour interval is 10 m d^{-1} with thick contours -30, 0, and 30 m d^{-1}.

The IG2 vertical velocity fields, w_2^{2d} (Fig. 5) and w_2 (Fig. 6), have similar spatial scales and patterns as the QG/IG1 vertical velocity (Fig. 3). The signs of w_2^{2d} and w_2 match the sign of w_{qg} at 88% and 86% of the grid points, respectively. The general consensus within the literature states that w_{qg} is often qualitatively accurate in describing the actual vertical velocity (Davies-Jones 1991), but quantitatively w_{qg} tends to overestimate the actual vertical velocity (Pinot et al. 1996). Of the grid points where $|w_{qg}| > |w_2|$, the IG2 vertical velocity field

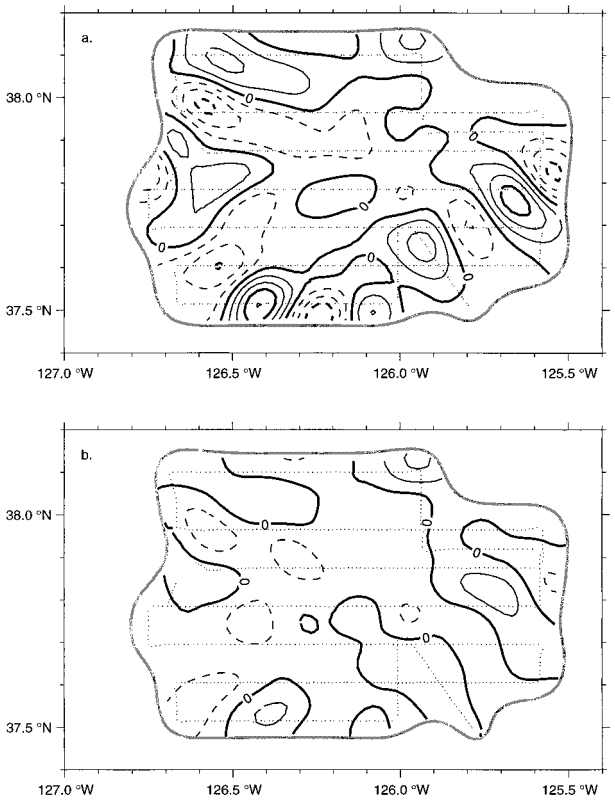

FIG. 6. IG2 vertical velocity w_2 (m d^{-1}) diagnosed, using the full forcing of the IG2 omega equation (22), at (a) 100 m and (b) 200 m. Contour interval is 10 m d^{-1} with thick contours −30, 0, and 30 m d^{-1}.

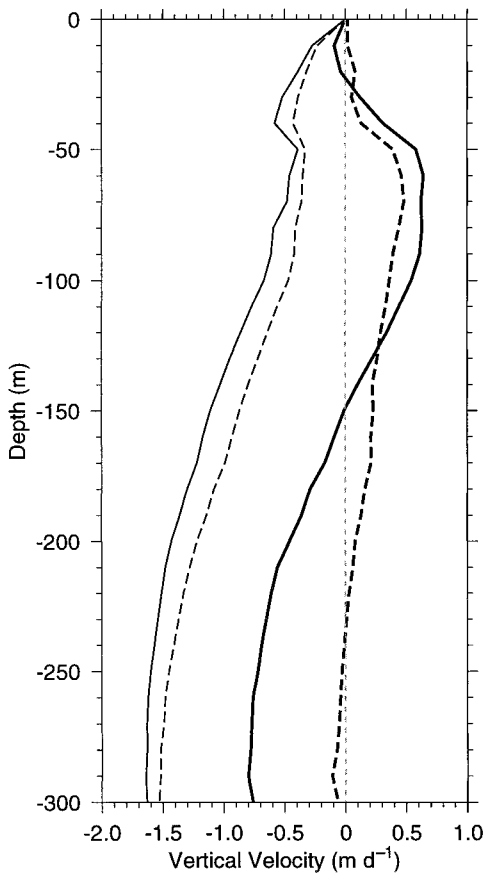

FIG. 7. Area-averaged vertical velocity (m d^{-1}) computed via (23) for w_1 (thick solid line), w_2^{2d} (thin dashed line), w_2 (thin solid line), and w_{pe} (thick dashed line).

shows 36% weaker downwelling velocities and 45% weaker upwelling velocities. The maximum upwelling and downwelling velocities for w_2 and w_2^{2d} are shown in Table 1. The absolute maximum upwelling and downwelling velocities for w_2 and the maximum upwelling velocity for w_2^{2d} are greater than the QG maxima. However, those maxima occur over a smaller area (cf. Fig. 3, Fig. 5, and Fig. 6).

Area-averaged vertical velocity at a given depth is computed via

$$\overline{w}(z) = \frac{1}{A}\int w(x, y, z)\, dA, \qquad (23)$$

where A is the total area over which the vertical velocity is acting (always constrained to lie within the 10% error covariance). Area-averaged upwelling (downwelling) is computed from (23) over the area (A) where $w > 0$ ($w < 0$). The maximum area-averaged upwelling and downwelling velocity for w_2 and w_2^{2d} is less than w_{qg}. The area-averaged vertical velocity for both w_2^{2d} and w_2 is downwelling at all depths (Fig. 7), and the magnitude of the area-averaged vertical velocity increases with depth. This reinforces the view of a developing low-pressure cyclone as a horizontally convergent, net-downwelling feature (see Gill 1982, section 12.10). The area-averaged QG vertical velocity (Fig. 7) is positive (net upwelling) above 150 m, reaching a positive maximum at 70 m. The area-averaged QG vertical velocity gradient implies divergence above 70 m and convergence below, while the IG2 area-averaged vertical ve-

TABLE 1. Vertical velocity comparison.

	max w (m d^{-1})	max $\overline{w}$ (m d^{-1})	avg w (m d^{-1})	min $\overline{w}$ (m d^{-1})	min w (m d^{-1})
w_{qg}	39.0 (90 m)	11.8 (80 m)	−0.8 (290 m)	−10.8 (80 m)	−45.8 (40 m)
w_2	45.2 (80 m)	9.7 (70 m)	−2.0 (220 m)	−9.4 (80 m)	−50.4 (50 m)
w_2^{2d}	48.0 (90 m)	9.7 (80 m)	−1.8 (260 m)	−9.6 (90 m)	−39.5 (80 m)
w_{pe}	34.2 (120 m)	10.1 (100 m)	−0.6 (200 m)	−9.3 (100 m)	−33.4 (100 m)

locity gradients imply convergence at all depths. The difference is due to the neglect of ageostrophic motion in the QG analysis. Because there is mean convergence and sinking motion in this cyclonic system (more evident in the higher-order estimates), one suspects that it may still be intensifying. This was confirmed by computing ζ_{0t} from (9) and ζ_{1t} from (16), which (averaged over the entire volume) were both positive.

Finally, using the diagnosed IG2 vertical velocity w_2, the total IG2 horizontal velocity can be computed. The divergent component is calculated from the IG2 continuity equation

$$\boldsymbol{\nabla} \cdot \mathbf{u}_2 = \varepsilon \nabla^2 \chi_2 = -\varepsilon w_{2z}, \tag{24}$$

using the same boundary conditions as when solving for χ_1. The rotational component is diagnosed from the divergence of the IG2 momentum equations

$$\begin{aligned} \nabla^2 \psi_2 = {} & \nabla^2 \phi - \varepsilon 2 J(\psi_{1x}, \psi_{1y}) \\ & + \varepsilon^2 \{\nabla^2 \chi_{1t} + J(\chi_1, \zeta_1) + \nabla^2 J(\psi_1, \chi_1) \\ & \quad - J(w_1, \psi_{1z})\} \\ & + \varepsilon^3 \left\{ \boldsymbol{\nabla} \cdot (w_1 \boldsymbol{\nabla} \chi_{1z}) + \frac{1}{2}(\chi_{1x}^2 + \chi_{1y}^2) \right\}, \end{aligned} \tag{25}$$

where only the $O(1)$ and $O(\varepsilon)$ terms have been retained. The IG1 rotational velocity is used as the boundary condition.

Similar three-dimensional circulation diagnostics can be formed from the other iterated geostrophic models ($n = 3, 4, \cdots$). For the purposes of this analysis, though, it is sufficient to stop at IG2, which incorporates the $O(\varepsilon, \varepsilon^2)$ corrections to QG dynamics that are the focus of this study.

c. Balance equations

The balance equations (Gent and McWilliams 1983) are a well-known and widely used intermediate model. Previous studies have shown the balance equations (BE) to be an accurate (in comparison to a PE model) representation of dynamics when Rossby numbers are moderate to large (Barth et al. 1990; Allen and Newberger 1993). In the case of a stationary, circular, barotropic vortex, the balance equations exactly reproduce the PE solution, namely the gradient wind balance (McWilliams and Gent 1980).

The balance equations are formulated via a systematic truncation, retaining only the $O(1)$ and $O(\varepsilon)$ terms, of the equations for the vertical component of relative vorticity and horizontal divergence (Gent and McWilliams 1983). The balance equations (inviscid, f plane) consist of the truncated vorticity and divergence equations

$$w_z = \zeta_t + J(\psi, \zeta) + \varepsilon \boldsymbol{\nabla} \cdot [w \boldsymbol{\nabla} \psi_z + \zeta \boldsymbol{\nabla} \chi], \tag{26}$$

$$\nabla^2 \psi = \nabla^2 \phi - \varepsilon 2 J(\psi_x, \psi_y) \tag{27}$$

along with the continuity, hydrostatic, and thermodynamic energy equations

$$w_z = -\nabla^2 \chi, \tag{28}$$

$$\phi_z = \theta, \tag{29}$$

$$Sw = -\theta_t - J(\psi, \theta) - \varepsilon[\boldsymbol{\nabla} \cdot (\theta \boldsymbol{\nabla} \chi) + (w\theta)_z], \tag{30}$$

where the velocity field has, once again, been decomposed into its divergent and rotational components, represented by the streamfunction ψ and potential function χ.

One benefit of the iterated geostrophic models is that, like QG, the basic variable is the pressure field ϕ. The basic variable of the balance equations, the streamfunction ψ, can be determined from the nonlinear balance equation (27) given the pressure field ϕ. This is a nonlinear partial differential equation (falling under the class of Monge–Ampere equations) and cannot be solved by conventional techniques. The solution of (27) is also subject to the solvability constraint

$$\frac{1}{2} + \nabla^2 \phi > 0, \tag{31}$$

which is exceeded in some parts of the dataset used in this analysis.

The solution procedure for the nonlinear balance equation (27) follows Arnason (1958). First, regions of the geostrophic relative vorticity field that do not meet the solvability condition are repeatedly smoothed by averaging the four nearest grid points, until the solvability condition is met everywhere. The solution of (27) is an iterative process where the balance equation is essentially linearized about the previous iteration

$$\begin{aligned} \nabla^2 \psi^m + \varepsilon \psi_{yy}^{m-1} \psi_{xx}^m + \varepsilon \psi_{xx}^{m-1} \psi_{yy}^m - \varepsilon 2 \psi_{xy}^{m-1} \psi_{xy}^m \\ = \nabla^2 \phi, \end{aligned} \tag{32}$$

where $m \geq 1$ is the iteration number and $\psi^0 = \phi$. The solution at each iteration is obtained via successive overrelaxation, and the geostrophic velocity field is used to provide the boundary condition. The solution is obtained at each vertical level and converges at $m \approx 15$.

Another option for determining the balance equation streamfunction would be to use the streamfunction determined from the objective analysis of the observed ADCP velocity field. While this avoids having to solve the nonlinear balance equation (27), it relies on the assumption that the streamfunction field is being accurately measured (i.e., that noise sources are inconsequential or filtered and that time-dependent changes are not significant). Determining ψ via (27) is used here to keep the comparisons between BE solutions and IG solutions more consistent.

Before forming the BE omega equation, the vorticity and density equations are rewritten as

$$(1 + \varepsilon \zeta) w_z = \zeta_t + \mathbf{u}_{3d} \cdot \boldsymbol{\nabla}_{3d} \zeta + \varepsilon (\boldsymbol{\nabla} w \cdot \boldsymbol{\nabla} \psi_z), \tag{33}$$

$$-(S + \varepsilon \theta_z) w = \theta_t + \mathbf{u} \cdot \boldsymbol{\nabla} \theta. \tag{34}$$

The BE omega equation is then formed by taking

$$\partial_z(33) - \nabla^2(34) + \partial_{zt}(27). \quad (35)$$

This procedure is similar to that used when forming the QG or IG omega equations, however, the new term $\partial_{zt}(27)$ is required to eliminate the time derivatives of vorticity and density. The BE omega equation (Gent and McWilliams 1983), with all terms involving w placed on the lhs, is

$$(S + \varepsilon\theta_z)\nabla^2 w + (1 + \varepsilon\zeta)w_{zz} + \varepsilon 2\nabla w \cdot \nabla\phi_{zz} - \varepsilon\nabla w \cdot \nabla\psi_{zz} - \varepsilon\nabla w_z \cdot \nabla\psi_z + \varepsilon^2 2w\partial_{zz}J(\psi_x, \psi_y) = \partial_z(\mathbf{u}\cdot\nabla\zeta) - \nabla^2(\mathbf{u}\cdot\nabla\theta) - \varepsilon 2\partial_{zt}J(\psi_x, \psi_y). \quad (36)$$

There are interesting similarities and differences between the BE omega equation and IG omega equations [IG1 (11); IG2 (20)]. The $\nabla^2 w$ term, rather than being scaled by S, is scaled by $S + \varepsilon\theta_z$, which is the horizontally variable N^2 (in dimensional terms). The inclusion of the horizontally variable N^2 has been used in previous QG diagnoses where it is not formally appropriate. The BE omega equation makes this clear and confirms the order of this term to be εS^{-1} (Shearman et al. 1999). The first-order forcing terms are identical to the terms in the IG omega equations, namely differential horizontal advection of relative vorticity and the negative Laplacian of thickness advection. The vertical advection of thickness and relative vorticity present in IG2 [(20) and (22)] have been moved to the lhs.

The BE omega equation (36) can be reformulated similarly to the IG2 omega equation (22) by moving a few of the terms on the lhs to the rhs:

$$\nabla^2 Sw + w_{zz} = \partial_z(\mathbf{u}_{3d}\cdot\nabla_{3d}\zeta) - \nabla^2(\mathbf{u}_{3d}\cdot\nabla_{3d}\theta) + \varepsilon\{\partial_z[2\partial_t J(\psi_x, \psi_y) + (\nabla w\cdot\nabla\psi_z) - \zeta w_z]\}. \quad (37)$$

The similarity of the BE omega equation to the IG2 omega equation (22) is clear with the primary forcing terms being the three-dimensional advection of relative vorticity and density. The similarity continues with the $O(\varepsilon)$ terms. The Jacobian term in (37)

$$\varepsilon 2\partial_{zt}J(\psi_x, \psi_y),$$

is analogous to the ζ_1' term in the IG2 omega equation (22). Another similarity between the forcing of the BE and IG2 omega equations is the inclusion of the stretching term ζw_z. A difference between the two omega equations appears in the tilting/twisting term on the rhs of (37) and (22). The IG2 omega equation includes tilting/twisting by the divergent horizontal velocity field, brought in as an $O(\varepsilon^2)$ term, while the BE omega equation includes tilting/twisting by the rotational velocity only.

The solution of the BE omega equation (37) requires an iterative procedure since some terms on the rhs contain the divergent velocity field (χ_x, χ_y, w). The forcing of (37) is computed using values of χ and w from the previous iteration, with $\chi^0 = w^0 = 0$. The time-derivative of ψ in the Jacobian term is diagnosed from the BE vorticity equation (26), where the divergent velocity field is determined from the previous iteration. Once the rhs is computed, the solution procedure is identical to the IG2 omega equation. The solution of the BE omega equation converges after approximately 13 iterations.

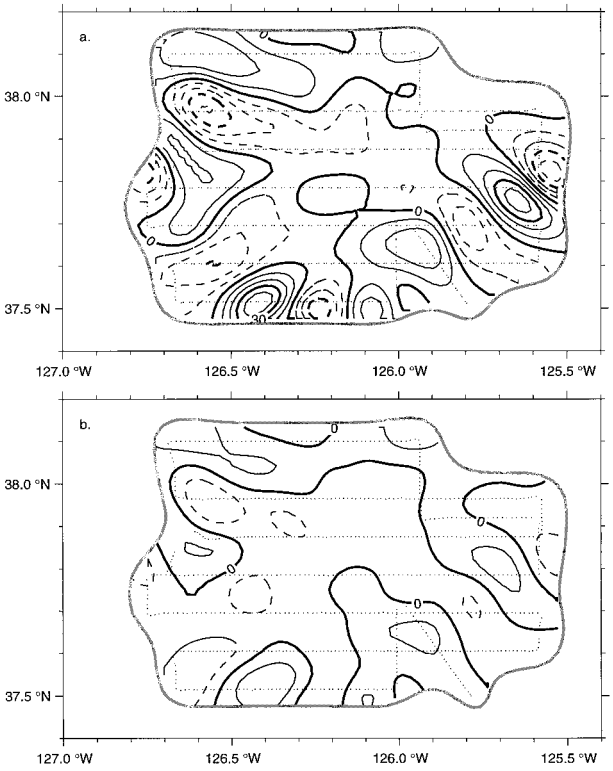

FIG. 8. The BE vertical velocity w_{be} (m d^{-1}) diagnosed via the BE omega equation (36) at (a) 100 m and (b) 200 m. Contour interval is 10 m d^{-1} with thick contours -30, 0, and 30 m d^{-1}.

The vertical velocity field w_{be} (Fig. 8) diagnosed from the BE omega equation (37) is similar in pattern and scale to the QG and IG2 vertical velocity fields. The signs of w_{be} and w_{qg} match at 88% of the grid points. Of the grid points where $|w_{qg}| > |w_{be}|$, the BE vertical velocity has 37% weaker upwelling velocities and 33% weaker downwelling velocities. The maximum BE upwelling velocity is 53 m d^{-1} and the maximum downwelling velocity is -48 m d^{-1}.

3. Primitive equation/digital filter initialization

An alternative method for diagnosing secondary circulation is achieved through the coupling of a primitive equation (PE) model and a low-pass digital filter, the so-called digital filter initialization (DFI). The DFI technique, developed for numerical weather prediction by Lynch and Huang (1992), involves the initialization of a PE model (Haney 1985) with the observed density and velocity fields, followed by short ($\leq$24 h) backward and forward integrations. The final diagnosed fields are then obtained by applying a low-pass filter to the re-

sultant time series. The hypothesis is that the system of equations within the PE model has an underlying ''slow manifold'' (Lorenz 1992) that can be recovered by removal of the high-frequency content. The PE/DFI technique is equivalent to nonlinear normal mode initialization (Lynch and Huang 1992). Since the DFI technique uses a PE model, the diagnosis of the three-dimensional circulation will necessarily include higher-order dynamics than those contained in QG.

This technique has been applied to quasi-synoptic CTD surveys in the Alboran Sea (Viúdez et al. 1996) and the California Current (Chumbinho 1994). The results were similar to the diagnosis of three-dimensional circulation using QG dynamics. Chumbinho (1994) analyzed a cyclonic eddy over the slope near Point Arena in May 1993—this is apparently the same eddy sampled in SS1 farther offshore as evident in a time series of satellite SST images (Kosro et al. 1994)—and concluded that the QG vertical velocities were 30% larger than the PE/DFI vertical velocities. This difference was attributed to the neglect of ageostrophic advection of relative vorticity and density.

The application of DFI to SS1 follows Chumbinho (1994) and Viúdez et al. (1996). The objectively analyzed density field and the geostrophic velocity field referenced to objectively analyzed ADCP data are used to initialize the PE model. Since the PE/DFI solution is obtained through the process of geostrophic adjustment, the initial currents significantly influence the solution only on scales comparable to, or less than, the Rossby radius. The geostrophic currents are used because the ageostrophic part of the analyzed ADCP currents are subject to significant noise sources on smaller scales (inertial motions and internal tides). The forward and backward integration time was 9 h (total integration time of 18 h), and the DFI was applied once. Using an 18-h filter span, inertial motions, having a period of about 19 h at 38°N, are partly removed (filter response ~0.6) and inertia–gravity waves, having periods much less than this, are completely removed (Viúdez et al. 1996). A variety of integration times and DFI applications were tested and compared. The results did not vary qualitatively for different integration times and number of applications of the DFI.

Observed small-scale meanders along the density front (Shearman et al. 1999) are similar to frontal instabilities that propagate rapidly in the direction of the mean flow (Barth 1994). These small-scale meanders can also be seen to propagate in the PE model (Fig. 9). The small-scale meanders are associated with strong vertical velocities (Shearman et al. 1999). The propagation of these meanders will affect the value of filtered fields. Thus, the choice of integration times will influence the results. From the prefiltered, time-dependent density field in the PE model (Fig. 9), the propagation of these instabilities can be tracked. Propagation speeds range from 0.13 to 0.32 m s^{-1}.

The filtered density field is slightly altered from its initial state (Fig. 2) due to the adjustment processes in the PE model. This adjustment is small; the rms difference between the original and filtered density fields is 0.007 kg m^{-3}. The DFI vertical velocity field (Fig. 10) is similar in pattern to the QG vertical velocity field. The maximum upwelling velocity is approximately 34 m d^{-1} and the maximum downwelling velocity is 33 m d^{-1} at about 100 m (see Table 1). Visually, there appears to be little difference between the QG and DFI vertical velocity fields, except for a general reduction in the magnitude of vertical velocity. As with the intermediate model diagnostics, the spatial patterns are quite similar; the sign of w_{be} matches the sign of w_{qg} at 84% of the

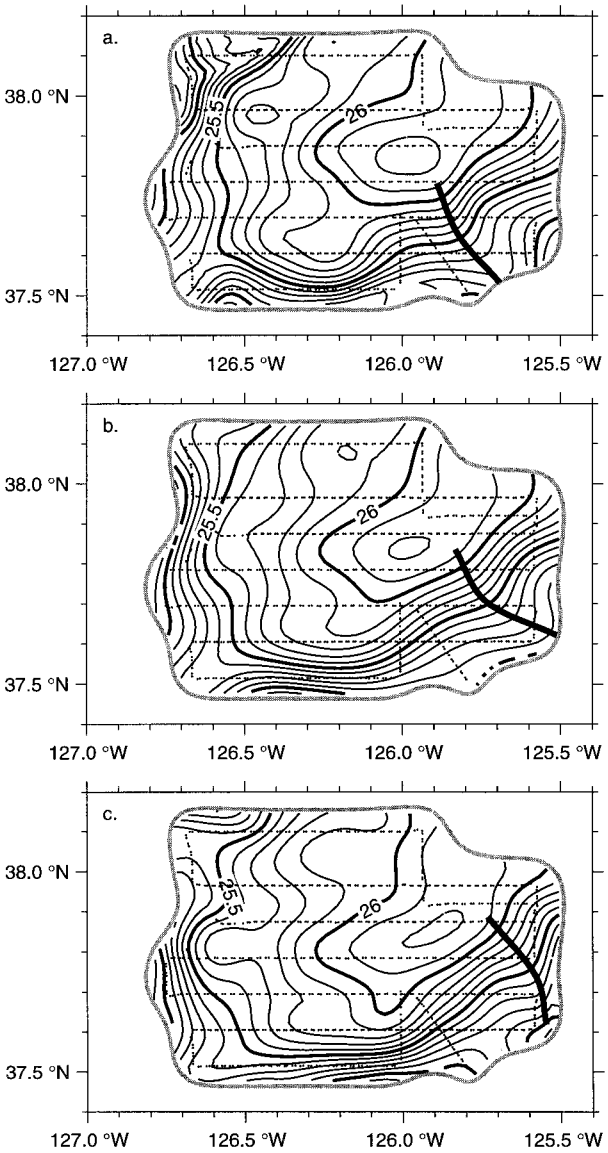

FIG. 9. Primitive equation model density fields σ_t^{pe} (kg m^{-3}) at 100 m from model time (a) $t = -9$ h, (b) $t = 0$ h, and (c) $t = 9$ h. The heavy line signifies the location and propagation along the front of a small-scale meander trough.

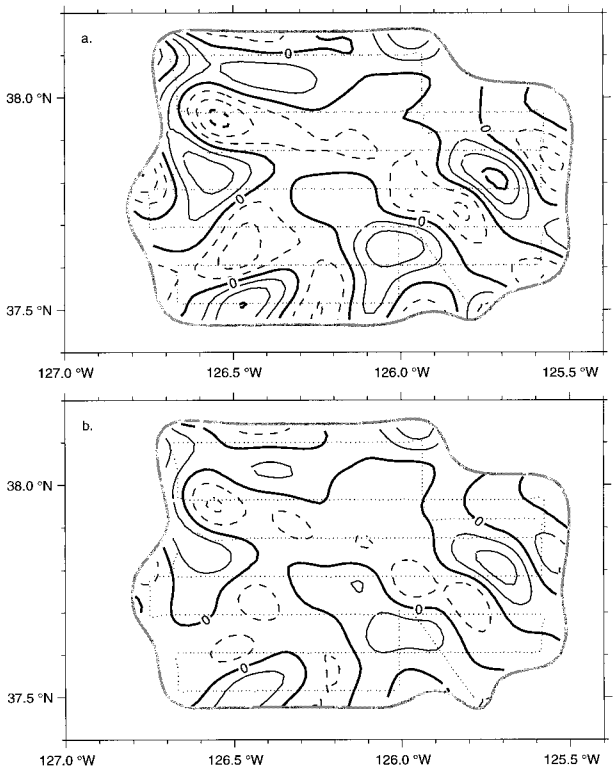

FIG. 10. Vertical velocity w_{pe} (m d^{-1}) diagnosed using the PE/DFI technique at (a) 100 m and (b) 200 m. Contour interval is 10 m d^{-1} with thick contours -30, 0, and 30 m d^{-1}.

grid points. Of the grid points with $|w_{qg}| > |w_{pe}|$, there is an average 36% reduction in w_{pe} for downwelling and 35% reduction for upwelling. The area-averaged PE vertical velocity (Fig. 7) is similar to the area-averaged QG vertical velocity.

4. Gradient wind

In order to explain the dynamics and the diagnostic estimates of secondary circulation, the simplest higher-order model, the gradient wind balance, is explored. At synoptic length scales, the primary balance of forces in the ocean is between the horizontal pressure gradient and the Coriolis forces, the geostrophic balance. The geostrophic balance is strictly applicable only to flow along straight dynamic height contours (Holton 1992). When dynamic height contours curve, the appropriate force balance is among the Coriolis, pressure gradient, and centrifugal forces—the gradient wind balance. In SS1, the strongly curved flow suggests the appropriateness of the gradient wind balance.

Using a natural coordinate system following Holton (1992), the cross-stream momentum balance for time-independent, two-dimensional flow parallel to dynamic height contours is

$$\frac{V^2}{R} + fV = -\frac{\partial \Phi}{\partial n}, \tag{38}$$

referred to as the gradient wind equation, where V is the horizontal speed (a positive definite scalar), Φ is the geopotential field, and R is the radius of curvature of the flow where $R > 0$ indicates cyclonic curvature (see appendix A for further definitions). The centrifugal force is given by V^2/R, the pressure gradient force is given by $-\partial\Phi/\partial n$, and the Coriolis force is fV. The geostrophic approximation

$$fV_g = -\frac{\partial \Phi}{\partial n}$$

is recovered from (38) as $R \to \pm\infty$ (flow without curvature), and the gradient wind equation can be rewritten

$$\frac{V^2}{R} + fV = fV_g. \tag{39}$$

For the following analysis, it is assumed that streamlines and water parcel trajectories are equivalent as would be the case for steady-state motion (Batchelor 1967). The effects of this assumption are quantifiable, with the primary error coming from the large-scale advection of the mesoscale pattern of streamlines (Holton 1992). When a steady state is assumed and the geopotential field is known, the radius of curvature for water parcel trajectories is completely determined (see appendix A). Given the geopotential field and the radius of curvature, the quadratic gradient wind equation (39) can be solved

$$V = \frac{-Rf}{2} \pm \left(\frac{R^2 f^2}{4} + RfV_g\right)^{1/2}. \tag{40}$$

By choosing to seek regular solutions (see appendix A) and defining a Rossby number based on radius of curvature

$$\varepsilon_R = \frac{V_g}{fR}, \tag{41}$$

the solution to the gradient wind equation becomes

$$V_{gw} = \frac{2V_g}{1 + (1 + 4\varepsilon_R)^{1/2}}, \tag{42}$$

for regions of both cyclonic and anticyclonic curvature (see appendix A for solution details). Regions of positive (negative) ε_R indicate cyclonic (anticyclonic) curvature.

The horizontal distribution of ε_R (Fig. 11c) is similar to the geostrophic and IG1 relative vorticity fields (Figs. 11a,b). The magnitude of ε_R is consistently weaker than the magnitude of ζ_g/f and ζ_1/f. This is to be expected because ε_R is an approximation to the curvature vorticity (the largest values of ε_R overlie the most strongly curved portions of the density front), and the difference then is due to shear vorticity. At 100 m, the maximum positive (negative) value of ε_R is 0.47 (-0.25) compared with values of maximum geostrophic relative vorticity (scaled by f) of 0.69 (-0.40). As mentioned in appendix

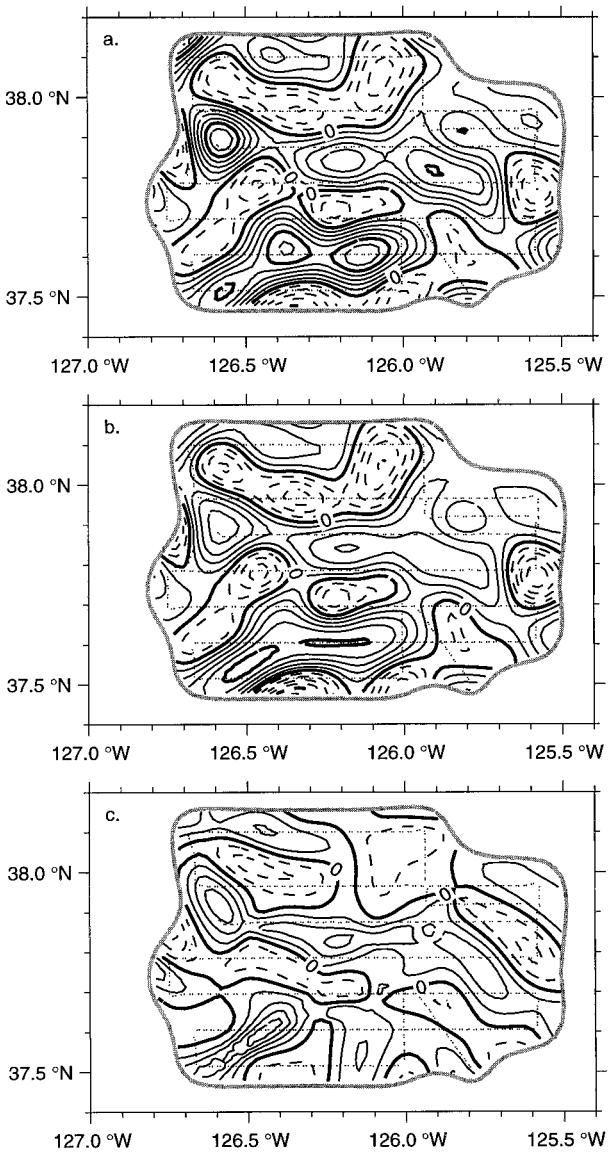

FIG. 11. (a) Geostrophic relative vorticity ζ_g scaled by f, (b) IG1 relative vorticity ζ_1 scaled by f, and (c) Rossby number ε_R estimated using the geostrophic velocity and objectively determined radius of curvature R, all at 100 m. Contour interval is 0.1 for all fields with thick contours at 0 and 0.5.

A, to assure real values for the velocity field in gradient wind balance, the magnitudes of negative ε_R are constrained to be no more than 1/4. For $\varepsilon_R < 0$ over the entire survey region, $|\varepsilon_R|$ exceeds 1/4 at only 3.7% of the grid points and exceeds 0.35 at 0.7%, all above 100 m. Near the surface, ε_R attains its largest values of 0.82 (40 m) and -0.53 (0 m). In the analysis presented here, the few grid points where $\varepsilon_R < 0$ and $|\varepsilon_R| > 1/4$ are reset to a maximum negative value of -0.25.

For SS1 at the surface, the gradient wind velocity $V_{\rm gw}$ is on average 0.12 m s^{-1} faster in anticyclonic regions ($\varepsilon_R < 0$) and 0.06 m s^{-1} slower in cyclonic regions ($\varepsilon_R > 0$) than V_g, with a maximum increase of 0.71 m s^{-1} and decrease of 0.19 m s^{-1}. At 100 m, the gradient wind velocity field is on average only 0.02 m s^{-1} faster and 0.02 m s^{-1} slower, with a maximum increase of 0.18 m s^{-1} and decrease of 0.07 m s^{-1}. The calculation of gradient wind velocity is sensitive to large values of negative ε_R; the gradient wind velocity $V_{\rm gw}$ rapidly approaches $2V_g$ as ε_R approaches -0.25 (Fig. A1). The maximum speed increase seen in the gradient wind velocity field corresponds to a region where $\varepsilon_R = -0.25$. By asserting the geostrophic momentum approximation (Hoskins 1975), an approximate gradient wind velocity—that is less sensitive to negative values of ε_R—can be computed (see appendix A). At the surface, this approximate gradient wind velocity field $V_{\rm gm}$ is on average 0.07 m s^{-1} faster in anticyclonic regions and 0.07 m s^{-1} slower in cyclonic regions, with a maximum increase of 0.42 m s^{-1} and decrease of 0.23 m s^{-1}, and, at 100 m, $V_{\rm gm}$ is on average 0.02 m s^{-1} faster and 0.02 m s^{-1} slower, with a maximum increase of 0.10 m s^{-1} and decrease of 0.08 m s^{-1}.

5. Discussion

To examine the relationship between the geostrophic and higher-order velocity fields, comparisons between the geostrophic relative vorticity and higher-order estimates of relative vorticity are made via scatterplots. There is a clear functional relationship between ζ_g and ζ_1 (Fig. 12a). At high positive values, ζ_1 is reduced in comparison with ζ_g and, at large negative values, ζ_1 is enhanced in comparison with ζ_g. Assuming the characteristic length scales remain similar in both the relative vorticity and velocity fields, the relative vorticity fields will be proportional to the velocity field; that is to say, stronger velocities will yield stronger relative vorticities and weaker velocities will yield weaker relative vorticities. In this manner, the relationship between ζ_g and ζ_1 is consistent with the gradient wind balance. The gradient wind in cyclonic curvature is subgeostrophic and yields weaker relative vorticities; gradient wind in anticyclonic curvature is supergeostrophic and yields stronger relative vorticities. The IG2 relative vorticity ζ_2 (25) shows a similar functional relationship with ζ_g (Fig. 12b), exhibiting larger enchancement/reduction than ζ_1. The relationship between the relative vorticity field calculated from gradient wind field

$$\zeta_{\rm gw} = \mathbf{k} \cdot \boldsymbol{\nabla} \times \mathbf{V}_{\rm gw}, \tag{43}$$

and ζ_g (Fig. 12d) is similar to the relationship between ζ_1 and ζ_g, again demonstrating the importance of gradient wind balance on the IG1 rotational velocity field. To quantify this similarity, the linear regression of $\zeta_{\rm gw}$ onto ζ_1 has a slope of 1.0103 and a correlation of 0.9724 at 100 m.

The relative vorticity field computed from the BE streamfunction is similarly related to the geostrophic relative vorticity (Fig. 12c). The gradient wind balance

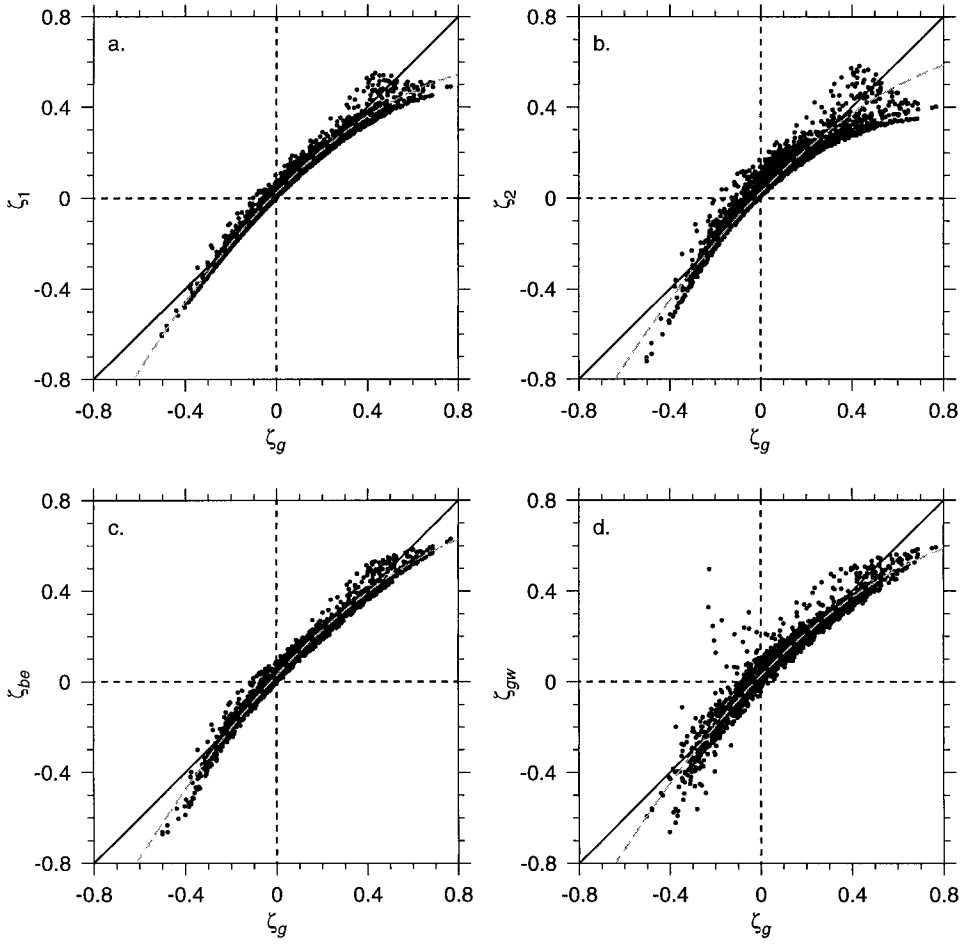

FIG. 12. Scatterplots at 100 m of dimensional values of geostrophic relative vorticity ζ_g versus (a) IG1 relative vorticity ζ_1 computed from (14), (b) IG2 relative vorticity ζ_2 computed from (25), (c) BE relative vorticity ζ_{be} computed from (27), and (d) gradient wind relative vorticity ζ_{gw}. The least-squares fit second-order polynomial is shown by the dashed gray line. The solid black line corresponds to a linear relationship with a slope of 1. All values of relative vorticity have been scaled by f.

is clearly reflected in the relationship between the BE relative vorticity ζ_{be} and ζ_g.

The horizontal velocity field diagnosed via the PE/DFI technique does not exhibit the gradient wind balance. There is little difference between ζ_{pe} and ζ_g (Fig. 13a). One reason for the discrepancy is that the component of the total velocity field in gradient wind balance is associated with fast propagating small-scale meanders, which were noted as being present by Shearman et al. (1999). These rapidly moving disturbances are filtered out by the DFI and, as such, not recognized as part of the slow manifold of the evolving flow field. Another possibility is the choice of initial velocity field. In this case, the initial velocity field is in geostrophic balance, computed from the initial density field. Thus, the initial velocity and density fields are already balanced and should not require much adjustment.

An initial velocity field in gradient wind balance would provide a different result. Therefore, the PE/DFI diagnosis was performed using the gridded density field and IG1 horizontal velocity as initial conditions. The resultant relative vorticity ζ_{pe}^{ig}, when compared to ζ_g (Fig. 13b), is different from ζ_{pe} initialized with the geostrophic velocity. There is a slight reduction (enhancement) in ζ_{pe}^{ig} apparent for large positive (negative) values of ζ_g. The effects of the filtering and adjustment processes within the model were to pull the initial velocity field (IG1) back toward the geostrophic velocity (cf. Fig. 13b and Fig. 12a). This is somewhat unexpected, since the IG1 horizontal velocity field is similar to the gradient wind velocity that is balanced with respect to the density (pressure) field, and therefore should not require much physical adjustment. The significance of this is that the gradient wind velocity may not be a part of the ''slow manifold'' within the PE model whenever, as in the present case, the largest gradient wind effects are associated with the small-scale, rapidly propagating frontal meanders. This highlights the greater requirement of the PE/DFI technique; the PE/DFI diagnosis requires both ρ and $\mathbf{u}$ as initial fields to provide an estimate of

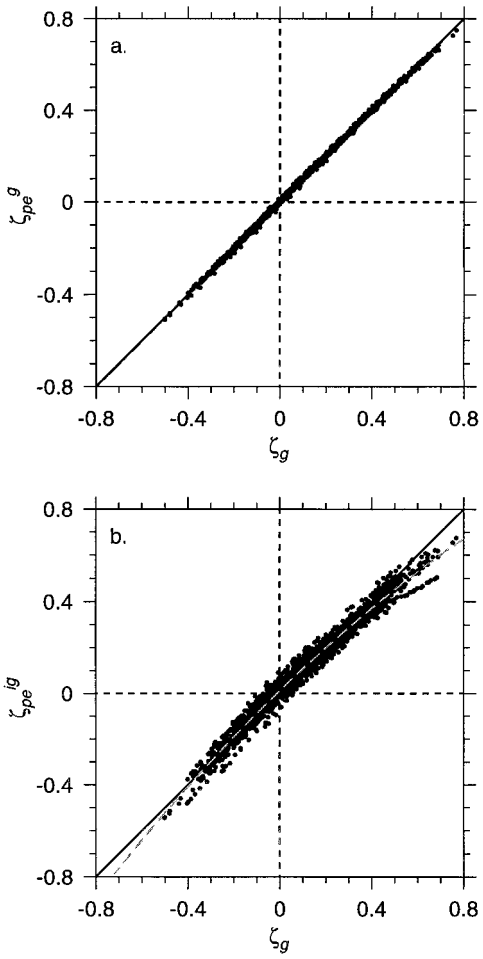

FIG. 13. Scatterplots at 100 m of dimensional values of geostrophic relative vorticity vs PE/DFI relative vorticity ζ_{pe} when the PE model is initialized using (a) the geostrophic velocity field and (b) the IG1 horizontal velocity field (divergent and rotational). The least-squares fit second-order polynomial is shown by the dashed gray line. The solid black line corresponds to a linear relationship with a slope of 1. All values of relative vorticity have been scaled by f.

w, whereas the QG and IG diagnoses require only ρ. The gradient wind velocity computed from (42) could also be used as an initial velocity field in the PE/DFI diagnosis.

The least-squares linear fits of w_2, w_2^{2d}, and w_{be} onto w_1 have slopes of 0.72, 0.76, and 0.98, respectively, at 100 m (Figs. 14a–c). This agrees with the general consensus that QG vertical velocities are overestimates of the actual vertical velocity. Although the slope of the linear fit of w_{be} onto w_1 is close to 1, similarities between the scatterplots of the IG vertical velocities and the BE vertical velocity indicate that w_{be} and w_2 relate similarly to the QG vertical velocity. Previously, differences between higher-order estimates of w and w_{qg} have been attributed to the ageostrophic advection of relative vorticity (Chumbinho 1994; Viúdez et al. 1996). By extending the same proportionality argument, previously applied to the relative vorticity, to the forcing of the IG2 omega equation, a reduction in the magnitudes of w_2 and w_2^{2d} compared with w_{qg} would only be expected in regions of cyclonic curvature, while an increase would be expected in regions of anticyclonic curvature. This is the result obtained by Moore and VanKnowe (1992). The reasoning behind this is that the forcing of the higher-order omega equation depends mainly on the horizontal advection of relative vorticity and thickness (in the case of w_2^{2d} the forcing depends entirely on horizontal advection) and, since the velocity field in gradient wind balance is reduced from the geostrophic for cyclonic features, advection will be similarly reduced. Conversely, advection in regions of anticyclonic curvature will be enhanced since the gradient wind velocities are supergeostrophic. Thus, extending the proportionality argument, higher-order vertical velocity estimates should be reduced compared with QG estimates in regions of cyclonic curvature and enhanced in regions of anticyclonic curvature. This disagrees with the general consensus that w_{qg} tends to overestimate everywhere.

The DFI diagnosed vertical velocities w_{pe} are generally reduced as well (Fig. 14d). The slope of the least-squares linear fit was 0.84, indicating a smaller reduction compared with the reduction from w_{qg} exhibited by the IG2 vertical velocities. The vertical velocity w_{pe}^{ig} diagnosed via the PE/DFI technique with the IG1 horizontal velocity field as an initial condition was only slightly different from w_{pe}. The slope of the least squares linear fit of w_{pe}^{ig} to w_{qg} was 0.86, and the average reduction in magnitude for both upwelling and downwelling was 31% for grid points where $|w_{qg}| > |w_{pe}^{ig}|$.

Although Lynch and Huang (1992) show that DFI is equivalent to NNMI, in all applications of DFI to relatively small scales (i.e., scales of the order of, or smaller than, the Rossby radius) a knowledge of the slow-mode currents for initial conditions is required. When, as in the present study, we use geostrophic currents at the initial time, the DFI technique treats these as valid independent estimates (observations) of the currents. The smaller-scale features in the initial analysis then adjust to these (geostrophic) currents during the PE model integration that is part of the DFI process. Since the larger-scale features, at least in the present situation, are rather well described by QG dynamics, a QG-like DFI solution (Fig. 9) is obtained.

It is therefore clear that the DFI diagnostic method cannot improve upon a QG estimate of vertical velocity without at least some information on the slow-mode currents at the initial time. To be specific, the method requires a good analysis of the rotational part of the ageostrophic, slow-mode currents on the smaller scales. However, even if this information is indeed available, the smaller space scales tend also to have shorter timescales and therefore they are partly removed by the DFI filter. From this discussion it is apparent that the IG and DFI diagnostic solutions primarily differ in how they

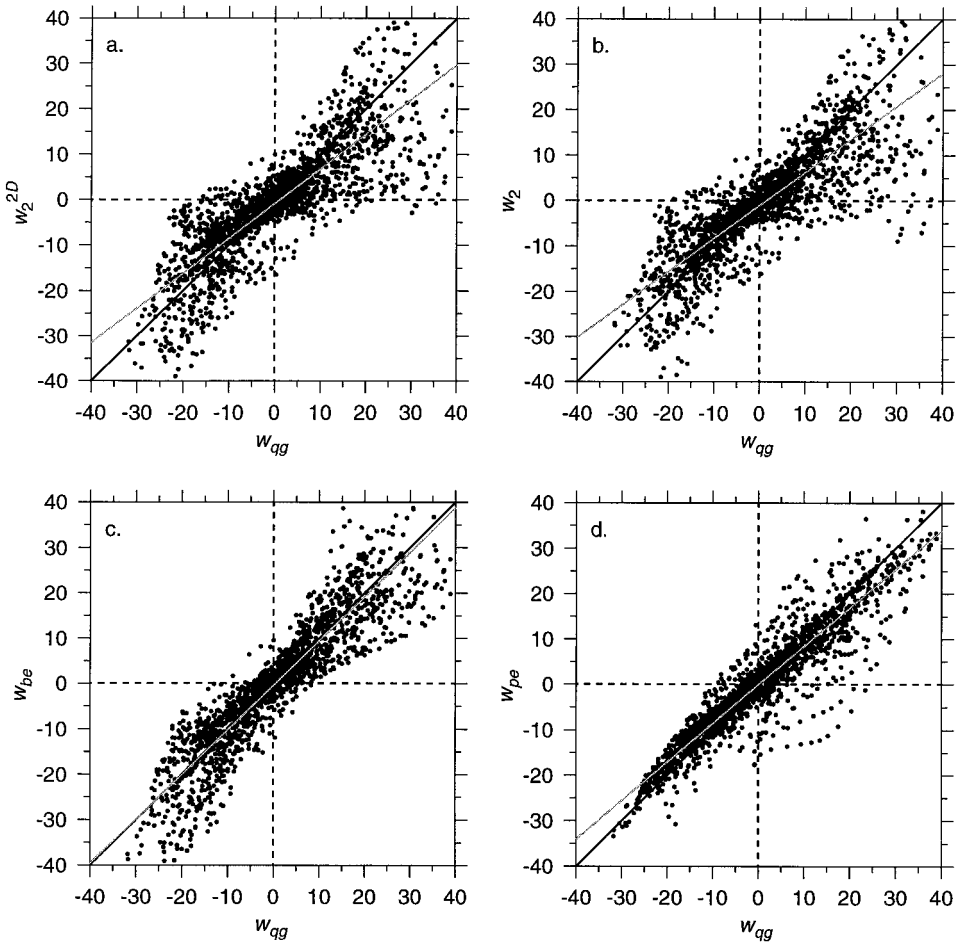

FIG. 14. Scatterplots at 100 m of QG vertical velocity w_{qg} vs (a) vertical velocity computed from (21), which contains only the $O(1)$ terms in the IG2 omega equation (20) w_2^{2d}, (b) vertical velocity computed from the full IG2 omega equation (22) w_2, (c) vertical velocity computed from the BE omega equation (36) w_{be}, and (d) vertical velocity computed via the PE/DFI technique w_{pe}, where the PE model is initialized with the geostrophic velocity field. The least-squares linear fit is shown by the dashed gray line. The solid black line corresponds to a linear relationship with a slope of 1.

treat the smaller scales. Here, the IG method produces a gradient balance current and a corresponding vertical velocity that is different from w_{qg}. The DFI method, on the other hand, partly damps such scales and, without accurate information about the ageostrophic nature of the currents, produces a QG-like solution. By keeping the analyzed mass field unchanged, the IG method essentially assumes that the smaller scales are a part of the slow mode. By contrast, the DFI method basically assumes (via the DFI filter) that the higher frequencies (smaller scales) are not entirely balanced and therefore not a part of the slow mode.

To further examine the influence of the gradient wind balance on the forcing of vertical velocity through advection, the geostrophic and ageostrophic advections of geostrophic and ageostrophic relative vorticity were monitored (Fig. 15a) along a geostrophic trajectory beginning at 100-m depth and 38.12°N, 126.03°W (Fig. 16a). For this comparison, the ageostrophic velocity and ageostrophic relative vorticity are defined as the IG1 field minus the geostrophic field. Clearly, the strongest contribution to relative vorticity advection is the geostrophic advection of geostrophic relative vorticity ($\mathbf{u}_g \cdot \nabla\zeta_g$), which in QG scaling is $O(1)$. As expected, the weakest contribution is the ageostrophic advection of ageostrophic vorticity ($\mathbf{u}_{ag} \cdot \nabla\zeta_{ag}$) which in QG scaling is $O(\varepsilon^2)$. The $O(\varepsilon)$ term $\mathbf{u}_{ag} \cdot \nabla\zeta_g$, which is the ageostrophic advection of geostrophic relative vorticity and would be the term expected to behave according to the proportionality argument above, is only slightly larger than the ageostrophic advection of ageostrophic relative vorticity and obviously not likely to influence the corresponding vertical velocity field. The other $O(\varepsilon)$ term, the geostrophic advection of ageostrophic relative vorticity ($\mathbf{u}_g \cdot \nabla\zeta_{ag}$) is much larger than ageostrophic advection of geostrophic relative vorticity. At times, the geostrophic advection of ageostrophic relative vorticity is equal in magnitude to the geostrophic advection of

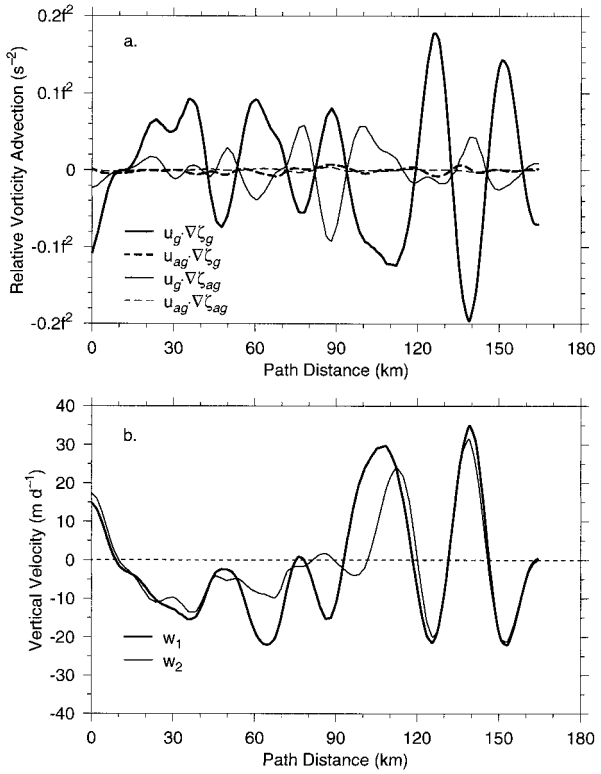

FIG. 15. (a) Comparison of relative vorticity advection along a geostrophic trajectory at 100 m. The subscript *g* indicates a geostrophic field and the subscript *ag* indicates an ageostrophic field, which is computed from the IG1 field minus the geostrophic field. (b) Comparison of vertical velocity along same trajectory.

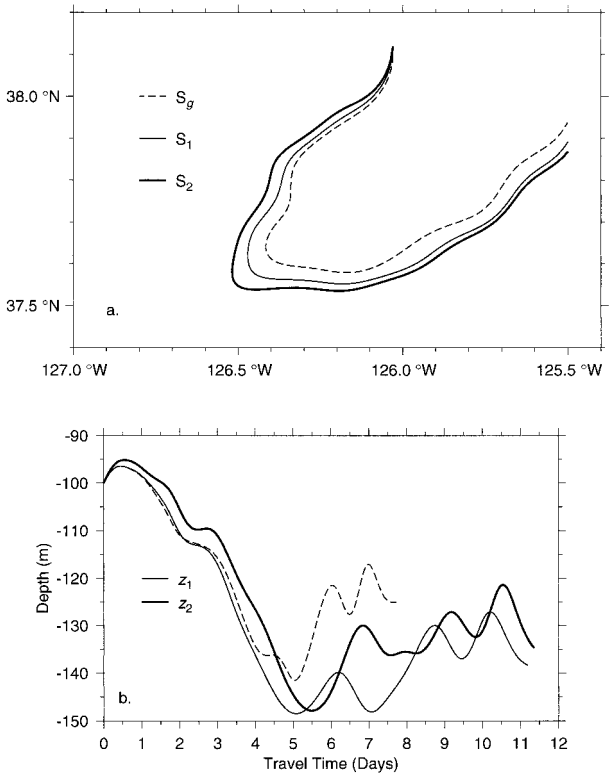

FIG. 16. (a) Water parcel trajectories computed from the geostrophic velocity field (dashed line), the IG1 total velocity field (thin solid line), and the IG2 total velocity field (thick solid line). (b) Net vertical displacement of water parcels moving with the IG1 total velocity field (thin solid line), the IG2 total velocity field (thick solid line), and determined by integrating the QG vertical velocity w_{qg} along a geostrophic trajectory as reported in Shearman et al. (1999) (dashed line).

geostrophic relative vorticity, e.g., between 70 and 90 km (Fig. 15a). Most significantly, the geostrophic advection of ageostrophic relative vorticity is almost always opposite in sign to the geostrophic advection of geostrophic relative vorticity. The net result is that the forcing of w by relative vorticity advection is reduced, regardless of curvature. In Fig. 15b, the influence of the geostrophic advection of ageostrophic relative vorticity is clear as seen by the difference between the QG vertical velocity and the higher-order vertical velocity w_2. The largest differences occur where geostrophic advection of ageostrophic relative vorticity is strongest and, in those regions, w_2 is always reduced in comparison with w_{qg}. This differs from the conclusions of Chumbinho (1994), who attributes the overestimation by QG vertical velocity to the neglect of ageostrophic advection in the QG diagnosis.

Water parcel trajectories (Fig. 16a) have been computed in an analogous fashion to Shearman et al. (1999). Trajectories were determined by linearly interpolating the velocity to the location of the water parcel and integrating, using a time step of 15 min (0.01 days), to find the water parcel's next location. The geostrophic trajectory $\mathbf{S}_g$ computed from the geostrophic velocity $(u_g, v_g, 0)$, constrained to a constant depth consistent with the QG approximation (Shearman et al 1999), is the shortest among the three and takes 7.7 days to traverse the survey region. Integrating w_1 along the level geostrophic trajectory yields a net vertical displacement of -20 m (Fig. 16b). Unlike Shearman et al. (1999), for the higher-order trajectories, the water parcels were not constrained to remain on a horizontal level, but rather were free to move in all three dimensions. The IG1 trajectory $\mathbf{S}_1$ computed from the IG1 velocity (u_1, v_1, w_1) is slightly longer than the geostrophic path and undergoes a net vertical displacement of -40 m. The IG1 water parcel takes 11.2 days to move through the region. The IG2 trajectory $\mathbf{S}_2$ computed from (u_2, v_2, w_2) is longest and undergoes a net vertical displacement of -35 m. The vertical displacements computed from w_1 and w_2 are quite similar with net sinking followed by net rising motion. The net vertical displacement from the IG2 vertical velocity is less than the QG net vertical displacement when both are computed along a common trajectory, for example, $\mathbf{S}_1$ (not shown). This is expected since $|w_2|$ is reduced in general compared with $|w_1|$.

The IG1 ageostrophic velocity (Fig. 17) exhibits three

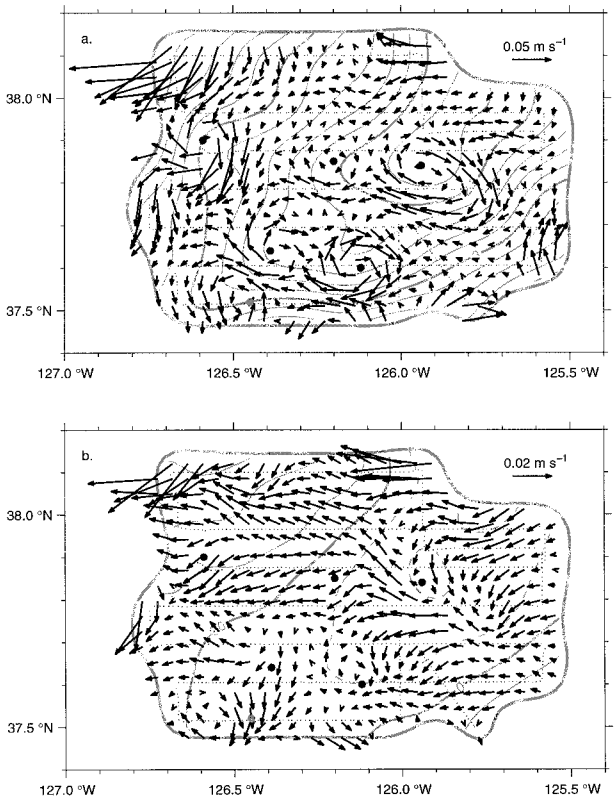

FIG. 17. The IG1 ageostrophic velocity (arrows) and dynamic height field ($m^2\ s^{-2}$) at (a) 100 m and (b) 200 m. Contour interval for dynamic height is 0.1 $m^2\ s^{-2}$ with thick contours at 2.5 and 3.0 $m^2\ s^{-2}$. Gray solid circles indicate the center position of ageostrophic vortices.

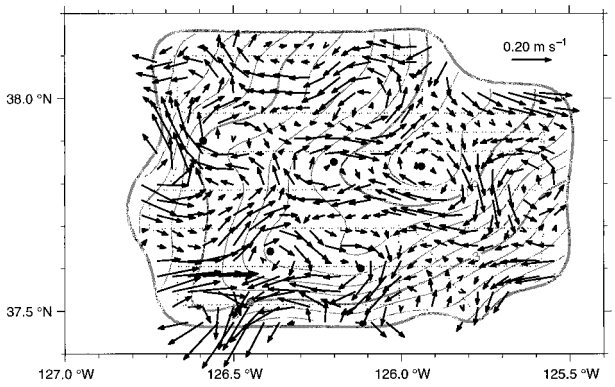

FIG. 18. The nondivergent ageostrophic velocity field (arrows), computed from the gridded ADCP data, and contours of dynamic height ($m^2\ s^{-2}$) at 100 m. Contour interval for dynamic height is 0.1 $m^2\ s^{-2}$ with thick contours at 2.5 and 3.0 $m^2\ s^{-2}$. Gray solid circles indicate the center position of ageostrophic vortices.

particular flow patterns; small-scale (diameter 10–15 km) vortices, flow along streamlines but opposing the main geostrophic current, and cross-frontal flow. The small-scale vortices are mostly anticyclonic and their position is associated with small-scale cyclonic curvature in the dynamic height (e.g., anticyclonic vortices at 37.85°N, 125.95°W; 37.90°N, 126.60°W; 37.60°N, 126.10°W; 37.65°N, 126.40°W; 37.85°N, 126.20°W; cyclonic vortex at 37.50°N, 126.45°W; all marked by gray dots in Fig. 17). The small-scale vortex flow is due entirely to the rotational component of the IG1 velocity field. The ageostrophic vortices are surface-enhanced features, with a maximum speed of 0.25 m s^{-1} at the surface and almost nonexistent at 200 m.

Opposing flow is linked to the small-scale vortex flow and occurs primarily at the peak of small-scale cyclonic troughs, where the vortex flow opposes the main geostrophic flow (e.g., 37.55°N, 126.15°W; 37.60°N, 126.45°W; and 37.75°N, 125.75°W). The absence of anticyclonic ageostrophic vortices at the peak of small-scale anticyclonic ridges is attributed to the generally smaller values of curvature in such regions due to the broad cyclonic nature of the main flow. Opposing flow is due entirely to the rotational component of the IG1 velocity field. Opposing flow in the IG1 ageostrophic velocity most closely resembles the ageostrophic velocity expected from gradient wind; along streamline and in opposition at cyclonic peaks.

Cross-frontal flow exhibits two characteristic length scales: a large scale associated with the primary cyclonic meander and a smaller scale associated with the ageostrophic vortices. In the northern part of the survey region near 38.0°N, 126.0°W, the large-scale cross-frontal flow at both 100 m and 200 m is westward, from more dense to less dense fluid. In the southeast (near 37.6°N, 125.8°W), the large-scale cross-gradient flow is directed northwestward, but the sense is now from less dense to more dense fluid. At 100 m, small-scale cross-frontal flow is evident. The small-scale cross-gradient flow is linked to the ageostrophic anticyclones such that cross-frontal flow is directed from less dense to more dense fluid on the upstream side and from more dense to less dense fluid on the downstream side. At 200 m, cross-frontal flow is the dominant ageostrophic flow pattern. The cross-gradient flow at 200 m is directed to the west-northwest and has a large, meander-wide scale. Cross-frontal flow is due mostly to the rotational velocity components; however, the divergent velocity also contributes, particularly at the large scale. At 200 m, the divergent and rotational components reinforce each other, directed primarily westward. At 100 m, the divergent flow opposes the rotational flow (cf. Fig. 4 with Fig. 17). At both 100 m and 200 m, the magnitude of the ageostrophic rotational velocity is two to three times the magnitude of the divergent velocity.

Observations of the nondivergent ageostrophic velocity field (Fig. 18), determined from the gridded shipboard ADCP velocity field minus the geostrophic velocity field, show similar circulation patterns as the IG1 ageostrophic velocity field (Fig. 17a). The gridded ADCP velocity field is constrained to be nondivergent through the objective analysis, so the ADCP ageostrophic velocity field is completely rotational, while the IG1

ageostrophic velocity field in Fig. 17a contains both divergent and rotational components. The rotational IG1 velocity component, though, is much larger than the divergent component. Anticyclonic vortices are located near the cyclonic meanders in the dynamic height field. At 100 m, the location of anticyclones in both fields is nearly one-to-one. The appearance of the predicted circulation patterns in an independent measure like the ADCP is strong corroboration of gradient wind balance in this feature and of the robustness of the higher-order vertical velocity diagnosis presented here. With this in mind, the ADCP velocity field can be used to represent the gradient wind velocity field in the gradient wind solution (42), and an independent estimate of the Rossby number based on R can be calculated from

$$\varepsilon_R^{\text{ADCP}} = \frac{V_g^2}{V_{\text{ADCP}}^2}\left(1 - \frac{V_{\text{ADCP}}}{V_g}\right)$$

and compared with $\varepsilon_R = V_g/fR$ (41). The two fields have a correlation of 0.80, and for anticyclonic values of $\varepsilon_R^{\text{ADCP}}$, the magnitude of $\varepsilon_R^{\text{ADCP}}$ never exceeds 1/4. Again, this gives strong support for gradient wind balance. This demonstrates that, given the appropriate circumstance (strong flow curvature), a shipboard ADCP is capable of measuring ageostrophic velocities. However, it is important to note that the divergent velocity component remains too small to be observed by the ADCP.

6. Conclusions

Two intermediate models, the iterated geostrophic models and the balance equations, and a primitive equation model coupled with a digital filter have been used to diagnose the ageostrophic flow fields (both horizontal and vertical) associated with a cyclonic jet meander in the CCS containing large Rossby number flow. The results show that including the dynamics of the gradient wind balance are important for ascertaining accurate estimates of the ageostrophic velocity field. In particular, the horizontal velocity field in gradient wind balance is subgeostrophic in cyclonic regions and supergeostrophic in anticyclonic regions. This relationship is seen in the IG1, IG2, and BE fields, and results in significant alteration of the relative vorticity. Higher-order estimates of vertical velocity are reduced in comparison with QG estimates for both upwelling and downwelling. This is shown to be primarily the result of the geostrophic advection of ageostrophic relative vorticity acting to reduce the net forcing of vertical velocity.

Vertical velocity diagnosed using the PE/DFI technique exhibits a reduction in comparison with w_{qg} as well. However, the diagnosed horizontal velocity field from the PE/DFI is almost entirely geostrophic. In this case, the PE model was initialized with the geostrophic velocity field, and only slight adjustment would be expected since the geostrophic velocity field is already in balance with the density field (on larger scales), needing only divergent motions to maintain a thermal wind balance. When the PE model was initialized with the IG1 horizontal velocity, the diagnosed horizontal velocity field differed from geostrophy, reflecting the gradient wind slightly. However, the diagnosed vertical velocity field was only slightly changed from w_{pe} initialized with the geostrophic velocity. The intermediate model and PE/DFI results differ in how they treat the smaller spatial scales; the intermediate models produce horizontal currents that reflect the gradient wind balance and vertical velocities that are correspondingly different from QG, while the PE/DFI solution tends to damp the horizontal velocities on smaller scales, treating them as not a part of the slow mode. Highly accurate observations of the initial slow-mode velocity field (with noise sources damped or removed) are the optimal choice for the PE/DFI diagnosis, and further study in this direction would prove useful.

A method to diagnose the gradient wind from a synoptic dynamic height field has been developed. This method provides an objective means for determining the radius of curvature of a water parcel trajectory, and requires only the assumption of a steady state (which is also assumed in the computation of the geostrophic wind).

Existence of a gradient wind balance and the success of the higher-order diagnosis is supported by observation from ADCP. The location of anticyclonic vortices associated with the gradient wind balance match on a nearly one-to-one basis between observations of the ageostrophic velocity field from ADCP and computation of the ageostrophic velocity field from IG1.

Acknowledgments. The authors would like to thank M. Kosro for his guidance on the treatment of the ADCP data and P. Velez for his assistance in the implementation of the primitive equation model and digital filter initialization. We thank J. McWilliams for his suggestion to more fully explore the balance equation solution and for his comments, along with those from an anonymous reviewer, that helped improve the manuscript. This work was supported by the Office of Naval Research through Grants N00014-92J1348 (RKS, JAB), N00014-97-1-0165 (RKS, JAB), N00014-93-1-1301 (JSA), and by an AASERT Grant N00014-93-1-0730 (RKS).

APPENDIX A

Estimating the Gradient Wind from Observations

The calculation of gradient wind requires knowledge of a water parcel trajectory (specifically the path curvature) and a choice between possible solutions of the quadratic gradient wind equation (39). In general, a synoptic hydrographic survey is not sufficient to determine a water parcel trajectory. However, by assuming a nondivergent steady state, a water parcel trajectory is completely determined by a streamline. Hence, the curvature

of the trajectory can be calculated from the dynamic height field. The choice of solutions to the quadratic gradient wind equation is indicated by the local Rossby number as well as physical considerations. Additionally, approximations can be made to extend the applicability of the gradient wind balance.

In order to describe the gradient wind balance, it is convenient to use a natural coordinate system following Holton (1992). The natural coordinate system is a locally rectangular coordinate system defined by the tangential and normal orthogonal unit vectors $\hat{\mathbf{t}}$ and $\hat{\mathbf{n}}$, where $\hat{\mathbf{t}}$ is directed parallel to the instantaneous velocity and $\hat{\mathbf{n}}$ is directed perpendicular with positive values to the left by convention. Following the trajectory of a water parcel, the velocity is expressed $\mathbf{V} = V\hat{\mathbf{t}}$, where $V = Ds/Dt$, s is distance traveled along the trajectory, and D/Dt is the material derivative following parcel motion. The speed V is always nonnegative. The acceleration of a water parcel is given by

$$\frac{D\mathbf{V}}{Dt} = \frac{DV}{Dt}\hat{\mathbf{t}} + \frac{V^2}{R}\hat{\mathbf{n}},$$

where the radius of curvature R is defined from the geometry of the water parcel trajectory as

$$\frac{D\hat{\mathbf{t}}}{Dt} = \frac{\hat{\mathbf{n}}}{R}.$$

Thus, given the trajectory of a water parcel

$$\mathbf{S}(t) = (x(t), y(t)), \tag{A1}$$

where x and y denote the water parcel location on a horizontal plane at time t (x and y must be continuous and at least twice differentiable), there exists a unique radius of curvature $R(t)$ at every point along the path defined by

$$R(t)^{-1} = \frac{\dot{x}\ddot{y} - \dot{y}\ddot{x}}{(\dot{x}^2 + \dot{y}^2)^{3/2}} \tag{A2}$$

where $(\cdot)$ indicates the total derivative D/Dt (McLenaghan and Levy 1996). The radius of curvature R is defined such that positive (negative) R corresponds to cyclonic (anticyclonic) curvature in the northern hemisphere. Typically, to find R the total derivatives must be evaluated, and even when this is possible, R is only defined in a Lagrangian sense along a specific trajectory. By assuming two-dimensional motion in a steady state

$$\frac{\partial}{\partial t} \to 0;$$

trajectories and streamlines become equivalent. The need to evaluate the Lagrangian total derivatives is thus eliminated, and R can be defined in an Eulerian sense. Given a synoptic streamfunction field (such as geopotential, dynamic height, or pressure) $\Phi = \Phi(x, y)$, the total derivatives are determined by the following relations:

$$\dot{x} = \frac{Dx}{Dt} = u = -\frac{\partial\Phi}{\partial y}, \qquad \dot{y} = \frac{Dy}{Dt} = v = \frac{\partial\Phi}{\partial x},$$

$$\ddot{x} = \frac{D^2x}{Dt^2} = \frac{Du}{Dt} = u\frac{\partial u}{\partial x} + v\frac{\partial u}{\partial y},$$

$$\ddot{y} = \frac{D^2y}{Dt^2} = \frac{Dv}{Dt} = u\frac{\partial v}{\partial x} + v\frac{\partial v}{\partial y}.$$

The radius of curvature can then be expressed in terms of the streamfunction field,

$$R(x, y)^{-1} = \frac{[(\Phi_y)^2\Phi_{xx} + (\Phi_x)^2\Phi_{yy} - 2\Phi_x\Phi_y\Phi_{xy}]}{[(\Phi_y)^2 + (\Phi_x)^2]^{3/2}}, \tag{A3}$$

or the nondivergent velocity field,

$$R(x, y)^{-1} = \frac{(u^2v_x - uv(u_x - v_y) - v^2u_y)}{(u^2 + v^2)^{3/2}}. \tag{A4}$$

This result is equivalent to the method used in Watts et al. (1995) to determine the curvature of the Z^*_{12} field (depth of the 12°C isotherm) in the Gulf Stream.

Once the radius of curvature R and geostrophic velocity $\mathbf{V}_g$ are known within a specific region, the gradient wind velocity $\mathbf{V}_{gw}$ can be computed via (40). First though, a choice must be made as to which root of the quadratic gradient wind equation is appropriate. For cyclonic curvature ($R > 0$), the solution is

$$V_{gw} = -\frac{fR}{2} + \frac{f|R|}{2}(1 + 4\varepsilon_R)^{1/2}, \tag{A5}$$

and for anticyclonic curvature ($R < 0$) the solution is

$$V_{gw} = -\frac{fR}{2} - \frac{f|R|}{2}(1 + 4\varepsilon_R)^{1/2}, \tag{A6}$$

where $f|R|/2$ has been factored out of the radical and ε_R has been substituted for V_g/fR. Both (A5) and (A6) correspond to the regular solutions, regular low ($R > 0$) and regular high ($R < 0$), discussed in Holton (1992). The anomalous solutions—anomalous low and anomalous high ($R < 0$ for both)—are excluded on the basis that the anomalous low is associated with very high Rossby number features such as tornados and the anomalous high is unlikely to occur far from the equator (Holton 1992). For $R < 0$, $|R| = -R$, which can be substituted into the anticyclonic solution, and, using $|R| = R$ for $R > 0$, both solutions can be written identically

$$V_{gw} = \frac{fR}{2}[(1 + 4\varepsilon_R)^{1/2} - 1]. \tag{A7}$$

Multiplying the rhs of (A7) by

$$\frac{(1 + 4\varepsilon_R)^{1/2} + 1}{(1 + 4\varepsilon_R)^{1/2} + 1},$$

we obtain V_{gw} in its final form (42). Since the gradient wind velocity must be real and nonnegative (by definition in the natural coordinate system), the solution (42) will be limited. Choosing the regular solutions en-

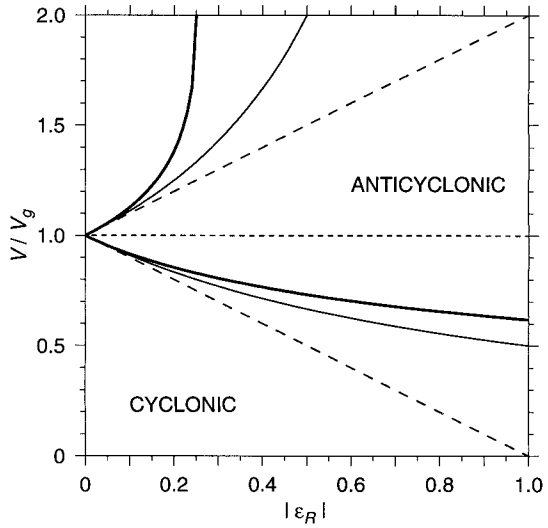

FIG. A1. The ratio of gradient wind to geostrophic wind V/V_g vs $|\varepsilon_R|$ found by solving (39). The solution to the exact gradient wind balance (heavy line) and approximate gradient wind balance, using the geostrophic momentum approximation (solid line) and the IG1 approximation (dashed line), are shown.

sures that $V_{\rm gw}$ will be nonnegative. To assure real valued solutions, the quantity $1 + 4\varepsilon_R$ must be nonnegative. For cyclonic curvature ($R > 0$), this will always be true, however, for anticyclonic curvature ($R < 0$), the Rossby number range is constrained to

$$|\varepsilon_R| \leq \frac{1}{4}.$$

The range of Rossby number can be extended by using some approximations to the gradient wind equation. The geostrophic momentum approximation to the gradient wind equation is

$$\frac{VV_g}{R} - fV = fV_g, \tag{A8}$$

(Hoskins 1975) where the cross-stream momentum attributable to centrifugal force is computed from the geostrophic velocity rather than the gradient wind velocity. Under the geostrophic momentum approximations, the solution is

$$V_{\rm gm} = \frac{V_g}{1 + \varepsilon_R}, \tag{A9}$$

and is applicable over a wider range of ε_R. In the geostrophic momentum approximation, there is no difference between geostrophic advection of centrifugal force due to gradient wind and gradient wind advection of centrifugal force due to geostrophic wind. The ratio of $V_{\rm gm}$ to V_g (Fig. A1) demonstrates the behavior of this solution as it varies with ε_R. For negative values of R, the solution is limited to the Rossby number range $-1 < \varepsilon_R \leq 0$.

For the IG1 approximation (13), the corresponding gradient wind equation is

$$\frac{V_g^2}{R} - fV = fV_g. \tag{A10}$$

In this case, the advection velocity is the geostrophic velocity and the momentum attributable to the centrifugal force is due to geostrophic velocity as well. The solution is

$$V_1 = V_g(1 - \varepsilon_R). \tag{A11}$$

For IG1, the solution is unrestricted for negative values of R, but for positive values of R, the Rossby number is limited to $0 \leq \varepsilon_R < 1$.

APPENDIX B

Dimensional Forms for the Iterated Geostrophic Diagnostic Equations

In the derivation of the higher-order omega equations, it was convenient to use nondimensional forms because they make explicit the order of the contributing terms. For the actual diagnosis applied to the in situ data, the corresponding dimensional forms were used. This appendix presents the dimensional forms used in the applied diagnosis. For the following equations, all variables are dimensional. In some cases, variable names may be the same as nondimensional variables. All fields estimated from the iterated geostrophic models that are plotted or mapped are dimensional.

The dimensional form for the IG1/QG omega equation (11) in its Q-vector formulation (12) is

$$\nabla^2(N^2 w_1) + f^2 \partial_{zz} w_1 = \nabla \cdot \mathbf{Q},$$

$$\mathbf{Q} = -2\frac{g}{\rho_0}(\partial_x \mathbf{u}_g \cdot \nabla\rho, \partial_y \mathbf{u}_g \cdot \nabla\rho), \tag{B1}$$

where $\mathbf{u}_g$ is the dimensional geostrophic velocity. The dimensional density ρ is defined

$$\rho(x, y, z, t) = \rho_0 + \overline{\rho}(z) - \theta(x, y, z, t),$$

where ρ_0 is the volume averaged density, $\overline{\rho}(z)$ is background stratification, and $\theta(x, y, z, t)$ is the negative perturbation density. The dimensional form for (14) the expression for the IG1 relative vorticity ζ_1 is

$$\zeta_1 = \nabla^2 \psi_1 = \zeta_g + \frac{2}{f} J(v_g, u_g), \tag{B2}$$

where ζ_g is the vertical component of the dimensional geostrophic relative vorticity field. The dimensional form for the boundary condition (15) used to solve for the IG1 streamfunction ψ_1 is

$$\mathbf{n} \cdot \nabla \psi_1 = \mathbf{k} \times \mathbf{n} \cdot \mathbf{u}_g. \tag{B3}$$

The dimensional form of the IG1 continuity equation is

$$\nabla \cdot \mathbf{u}_1 = \nabla^2 \chi_1 = - w_{1z}. \tag{B4}$$

The dimensional forms of the IG2 omega equations (21) and 22 are

$$\nabla^2(N^2 w_2^{2d}) + f^2 w_{2zz}^{2d} = f\partial_z(\mathbf{u}_1 \cdot \nabla\zeta_1) - \frac{g}{\rho_0}\nabla^2(\mathbf{u}_1 \cdot \nabla\rho) \quad \text{(B5)}$$

and

$$\nabla^2(N^2 w_2) + f^2 w_{2zz} = f\partial_z(\mathbf{u}_{3d1} \cdot \nabla_{3d}\zeta_1) - \frac{g}{\rho_0}\nabla^2(\mathbf{u}_{3d1} \cdot \nabla_{3d}\theta) + f\partial_z[\zeta_{1t}' + \mathbf{k} \cdot (\nabla w_1 \times \mathbf{u}_{1z}) - \zeta_1 w_{1z}], \quad \text{(B6)}$$

where $\mathbf{u}_1$ is the dimensional IG1 horizontal velocity field (both divergent and rotational), and $\mathbf{u}_{3d1}$ is the total dimensional velocity field. Note that in (B5) ρ can be used to compute the horizontal advection of density since no vertical derivatives occur, but in (B6) θ must be used to compute the density advection; otherwise vertical advection will be incorrect. The dimensional form for the expression of IG2 relative vorticity ζ_2 (25) is

$$\zeta_2 = \nabla^2\psi_2 = \zeta_g + \frac{2}{f}J(v_1, u_1), \quad \text{(B7)}$$

where the dimensional IG1 rotational velocity field is used to provide the gradient boundary condition. Finally, dimensional form for the IG2 continuity equation (24) is

$$\nabla \cdot \mathbf{u}_2 = \nabla^2\chi_2 = -w_{2z}. \quad \text{(B8)}$$

The dimensional form for the nonlinear balance equation (27) is

$$\zeta_{be} = \nabla^2\psi_{be} = \zeta_g + \frac{2}{f}J(\psi_{bex}, -\psi_{bey}), \quad \text{(B9)}$$

and the dimensional form for the BE omega equation (37) is

$$\nabla^2(N^2 w_{be}) + f^2 w_{bezz} = f\partial_z(\mathbf{u}_{3dbe} \cdot \nabla_{3d}\zeta_{be}) - \frac{g}{\rho_0}\nabla^2(\mathbf{u}_{3dbe} \cdot \nabla_{3d}\theta) + f\partial_z[\partial_t J(\psi_{bex}, -\psi_{bey}) + (\nabla w_{be} \cdot \nabla\psi_{bez}) - \zeta_{be} w_{bez}]. \quad \text{(B10)}$$

REFERENCES

Allen, J. S., 1993: Iterated geostrophic intermediate models. *J. Phys. Oceanogr.,* **23,** 2447–2461.

——, and P. A. Newberger, 1993: On intermediate models for stratified flows. *J. Phys. Oceanogr.,* **23,** 2462–2486.

Allen, J. T., and D. A. Smeed, 1996: Potential vorticity and vertical velocity at the Iceland–Færoes Front. *J. Phys. Oceanogr.,* **26,** 2611–2634.

Arnason, G., 1958: A convergent method for solving the balance equation. *J. Meteor.,* **15,** 220–225.

Barth, J. A., 1994: Short-wavelength instabilities on coastal jets and fronts. *J. Geophys. Res.,* **99,** 16 095–16 115.

——, J. S. Allen, and P. A. Newberger, 1990: On intermediate models for barotropic continental shelf and slope flow fields. Part II. Comparison of numerical model solutions in doubly-periodic domains. *J. Phys. Oceanogr.,* **20,** 1044–1076.

Batchelor, G. K., 1967: *An Introduction to Fluid Dynamics.* Cambridge University Press, 615 pp.

Bretherton, F. P., R. E. Davis, and C. B. Fandry, 1976: A technique for objective analysis and design of oceanographic experiments applied to MODE-73. *Deep-Sea Res.,* **23,** 559–582.

Chumbinho, R. P. A., 1994: Kinematics and dynamics of a cyclonic eddy off Point Arena, California. Ph.D. dissertation, Naval Postgraduate School, 83 pp.

Davies-Jones, R., 1991: The frontogenetical forcing of secondary circulations. Part I: The duality and generalization of the Q vector. *J. Atmos. Sci.,* **48,** 497–509.

Gent, P. R., and J. C. McWilliams, 1983: Consistent balanced models in bounded and periodic domains. *Dyn. Atmos. Oceans.,* **7,** 67–93.

Gill, A. E., 1982: *Atmosphere–Ocean Dynamics.* 1st ed. Academic, 662 pp.

Haney, R. L., 1985: Midlatitude sea surface temperature anomalies: A numerical hindcast. *J. Phys. Oceanogr.,* **26,** 706–724.

Holton, J. R., 1992: *An Introduction to Dynamic Meteorology.* 3d ed. Academic, 511 pp.

Hoskins, B. J., 1975: The geostrophic momentum approximation and the semi-geostrophic equations. *J. Atmos. Sci.,* **32,** 233–242.

——, and I. Draghici, 1977: The forcing of ageostrophic motion according to the semi-geostrophic equations and in an isentropic coordinate model. *J. Atmos. Sci.,* **34,** 1859–1867.

——, ——, and H. C. Davies, 1978: A new look at the ω-equation. *Quart. J. Roy. Meteor. Soc.,* **104,** 31–38.

Huyer, A., J. A. Barth, P. M. Kosro, R. K. Shearman, and R. L. Smith, 1998: Upper-ocean water mass characteristics of the California Current, summer 1993. *Deep-Sea Res. II,* **45,** 1411–1442.

Keyser, D., B. D. Schmidt, and D. G. Duffy, 1992: Quasigeostrophic diagnosis of three-dimensional ageostrophic circulations in an idealized baroclinic disturbance. *Mon. Wea. Rev.,* **120,** 698–730.

Kosro, P. M., and A. Huyer, 1986: CTD and velocity surveys of seaward jets off northern California, July 1981 and 1982. *J. Geophys. Res.,* **91,** 7680–7690.

——, ——, J. A. Barth, R. L. Smith, and P. T. Strub, 1994: Eddies in the California Current region off northern California from satellite and SeaSoar/ADCP measurements. *Eos, Trans. Amer. Geophys. Union,* **75** (3), 141.

——, J. A. Barth, J. Fleischbein, A. Huyer, R. O'Malley, K. Shearman, and R. L. Smith, 1995: SEASOAR and CTD observations during EBC cruises W9306A and W9308B June to September 1993. Data Report 160, Reference 95-2, College of Oceanic and Atmospheric Sciences, Oregon State University, Corvallis, OR, 393 pp.

Lorenz, E. N., 1992: The slow manifold—What is it? *J. Atmos. Sci.,* **49,** 2449–2451.

Lynch, P., and X.-Y. Huang, 1992: Initialization of the HIRLAM model using a digital filter. *Mon. Wea. Rev.,* **120,** 1019–1034.

McLenaghan, R., and S. Levy, 1996: Geometry. *CRC Standard Mathematical Tables and Formulae,* D. Zwillenger, Ed., CRC Press, 249–330.

McWilliams, J. C., and P. R. Gent, 1980: Intermediate models of planetary circulation in the atmosphere and ocean. *J. Atmos. Sci.,* **37,** 1657–1678.

Moore, J. T., and G. E. VanKnowe, 1992: The effect of jet-streak curvature on kinematic fields. *Mon. Wea. Rev.,* **120,** 2429–2441.

Onken, R., J. Fischer, and J. D. Woods, 1990: Thermohaline fine-structure and its relation to frontogenesis dynamics. *J. Phys. Oceanogr.,* **20,** 1379–1394.

Pedlosky, J., 1987: *Geophysical Fluid Dynamics.* Springer-Verlag, 710 pp.

Pinot, J.-M., J. Tintoré, and D.-P. Wang, 1996: A study of the omega equation for diagnosing vertical motions at ocean fronts. *J. Mar. Res.,* **54,** 239–259.

Rudnick, D. L., 1996: Intensive surveys of the Azores Front. Part II: Inferring the geostrophic and vertical velocity fields. *J. Geophys. Res.,* **101,** 16 291–16 303.

Shearman, R. K., J. A. Barth, and P. M. Kosro, 1999: Diagnosis of the three-dimensional circulation associated with mesoscale motion in the California Current. *J. Phys. Oceanogr.,* **29,** 651–670.

Strub, P. T., P. M. Kosro, and A. Huyer, 1991: The nature of the cold filaments in the California Current system. *J. Geophys. Res.,* **96,** 14 743–14 768.

Viúdez, A., R. L. Haney, and J. Tintoré, 1996: Circulation in the Alboran Sea as determined by quasi-synoptic hydrographic observations. Part II: Mesoscale ageostrophic motion diagnosed through density dynamical assimilation. *J. Phys. Oceanogr.,* **26,** 706–724.

Walstad, L. J., J. S. Allen, P. M. Kosro, and A. Huyer, 1991: Dynamics of the coastal transition zone through data assimilation studies. *J. Geophys. Res.,* **96,** 14 959–14 977.

Watts, D. R., K. L. Tracey, J. M. Bane, and T. J. Shay, 1995: Gulf Stream path and thermocline structure near 74°W and 68°W. *J. Geophys. Res.,* **100,** 18 291–18 312.